An elastic rod in frictional contact with a rigid cylinder

Paul Grandgeorge, Tomohiko G. Sano, Pedro M. Reis *

Flexible Structures Laboratory, Institute of Mechanical Engineering, École polytechnique fédérale de Lausanne, Switzerland

ARTICLE INFO

ABSTRACT

We investigate the load transmission along an elastic rod of finite cross-section in contact with a rigid cylinder, as system often referred to as the *generalized capstan problem*. In the presence of friction, the idealized classic capstan equation predicts that the tension along a perfectly thin and flexible filament increases exponentially along the contact region. In practical applications, however, the validity of the idealized capstan equation is compromised due to the interplay between finite rod thickness, bending stiffness, and the forces applied at the rod extremities. Here, we combine precision model experiments, finite element simulations, and theoretical modeling to investigate the contact mechanics and the force transmission along an elastic rod in frictional contact with a rigid cylinder. We study two cases when the rod is either static or sliding. First, we focus on the static case, in the absence of friction, by considering equal loads at both extremities of the rod. We show that as the loading force is increased, the nature of contact transitions from a localized region to an extended band at the surface of the cylinder. The latter is characterized by double-peaked contact force distribution. In the sliding case, friction is activated by inducing a relative motion between the rod and the cylinder. We applied a fixed loading force at one rod extremity while pulling the other extremity at a constant velocity. The driving force is monitored during sliding. For increasing loading forces, we find that the force ratio is non-monotonic and displays a local minimum, in contradiction with the constant ideal capstan prediction. This minimum force ratio coincides with the transition from a single contact point to an extended contact region. A theoretical analysis based on Euler's elastica serves to rationalize the results from the physical and numerical experiments. In addition to predicting the nature of the contact region (single point versus extended line), our model provides quantitative predictions for the wrapping angle and the driving-to-loading force ratio. Finally, we leverage our mechanics-based framework to predictively understand the force ratio at the ends of two commercially available engineering belts (spring-steel and polyurethane) in sliding contact with a steel cylinder.

1. Introduction

The load transmission along flexible filaments in frictional contact plays an important role in setting the mechanics of everyday filamentary structures such as knits (Poincloux et al., 2018; Bueno and Camillieri, 2019), woven fabrics (Ayres et al., 2018; Vekhter et al., 2019), and knots (Baek et al., 2020; Johanns et al., 2021; Patil et al., 2020; Maddocks and Keller, 1987; Audoly et al., 2007; Jawed et al., 2015; Daily-Diamond et al., 2017). More generally, the regions of contact between deformable elongated structures strongly influence the mechanical response of gridshells and triaxial weaves (du Peloux et al., 2013; Baek et al., 2018; Baek and Reis, 2019; Baek et al., 2021), mechanics of a snap-fit (Yoshida and Wada, 2020), stacks of deformable sheets (Poincloux

---

et al., 2021), climbing plants (Goriely and Neukirch, 2006), lubricated fibers on cylinders (Tu and Fort, 2004), filament and wire bundles (Grandgeorge et al., 2021; Stoop et al., 2008; Grason, 2009; Ward et al., 2015; Panaitescu et al., 2017, 2018; Warren et al., 2018), and can lead to snap-through buckling in the frictional elastica (Sano et al., 2017). In engineering applications, the frictional interaction between deformable belts and pulleys is commonly leveraged to enable power transmission between rotating shafts (Childs, 2019; Baser and Konukseven, 2010). Typically, the belt is wrapped around a rotating motor pulley, and the difference in tension of both belt strands drives the motion of a second pulley. When this tension difference exceeds a threshold value, the belt starts slipping on one of the pulleys, an undesirable effect that can lead to rotation desynchronization.

The classic *capstan equation*, also known as the Euler–Eytelwein equation, offers a description for the force transmission along a flexible filament or belt sliding in frictional contact with a cylinder. Euler (1769) and Eytelwein (1832) first derived the equations governing the difference in tension at both extremities of a sliding filament of vanishing thickness and bending stiffness. This canonical framework predicts the ratio between the (high) driving force, F_L, and the (low) loading force, F_0 applied at the extremities of the filament,

$$\frac{F_L}{F_0} = e^{\mu \Delta \alpha}, \tag{1}$$

where $\Delta\alpha$ is the wrapping angle of the filament around the cylinder, dictated by the orientation of the forces F_L and F_0, and μ is the kinematic friction coefficient. This capstan equation is often employed to predict the mechanical behavior of textiles (Shiryaev and Orlik, 2015) and has been adapted to predict the stability of knots (Maddocks and Keller, 1987). In addition, this model has been used to determine the frictional properties of natural fibers made out of wool, mohair, or cotton yarns (Martin and Mittelmann, 1946; Howell, 1953; Breazeale, 1947), and even synthetic flossing threads on teeth (Alali et al., 2018).

Even if idealized, Eq. (1) provides an accurate prediction of the driving-to-loading force ratio in the limits of negligible filament thickness compared to the cylinder diameter, and vanishing bending stiffness. In some applications, however, these two physical quantities cannot be neglected. For example, in the context of textiles or knots, contact takes place between flexible filaments wrapped around other filaments of the same diameter. Besides, in the engineering context of belt-on-pulley applications, belts often have a non-negligible bending stiffness. To bridge the gap between the assumptions of the idealized capstan framework and practical physical settings, previous theoretical studies have proposed enhanced models, which include the elasticity and the finite thickness of the rod sliding on the cylinder (Jung et al., 2004, 2008b; Stuart, 1961).

The effect of a finite bending stiffness of the rod in a capstan setting was first discussed by Stuart (1961), where an elastic filament of vanishing cross-sectional thickness was considered. In this case, the orientations of the forces applied at both extremities do not impose the wrapping angle, $\Delta\alpha$, of the contact geometry. Indeed, since the elastic rod can support internal shear forces, the tangent of the rod at the locations of touch-down and lift-off (*i.e.*, where the rod enters and leaves contact from the cylinder surface, respectively) is not necessarily aligned with the forces applied at the rod extremities. More specifically, Stuart (1961) first described the case when the rod only has a single contact point with the cylinder, showing that, if the opening angle between the loading and driving forces is larger than 120°, the classic capstan equation still provides an accurate prediction of the force ratio. In the case of an extended contact line (contact over an arc), Stuart (1961) suggested that, in addition to the well-known distributed forces applied by the cylinder onto the rod, some concentrated *point* forces may arise at the locations of touch-down and lift-off, and must be taken into account. Despite the presence of these concentrated forces, the author shows that the classic capstan equation, Eq. (1), yields an accurate description for the force ratio, provided the two forces applied at the rod extremities are larger than $\sim 400 EI/D^2$, where EI is the bending stiffness of the elastic filament and, D, the diameter of the rigid cylinder. Overall, Stuart (1961) suggests that the effect of bending stiffness only induces a small correction to the classic capstan equation.

The effect of the finite rod thickness on the load transmission in the contact region was later investigated extensively by Jung et al. (2004, 2008b) through analytical methods. When the rod has a non-zero thickness, these authors showed that, a relation for the balance of moments needs to be considered, in addition to the local force balance along the rod. Considered both force and moment balance, their theoretical predictions pointed to a significant decrease of the force ratio, F_L/F_0, for decreasing diameters of the rigid cylinder. However, this study overlooked the need to consider the presence of concentrated (point) forces applied onto the rod at locations of touch-down and lift-off, as had previously been suggested by Stuart (1961).

Although the studies by Stuart (1961) and Jung et al. (2004, 2008b) provided valuable insight into the mechanics of elastic rods on cylinders, a straightforward comparison between their models, as well as to experimental results, is challenging. In these theoretical studies, the extent of the contact region is assumed to be known *a priori*, appearing as a control parameter. In addition, the angle between the forces applied at the rod extremities and the angles at touch-down and lift-off are also assumed to be known. However, in the physical generalized capstan system, the wrapping angle and the orientation of the forces are usually part of the set of *unknowns* of the problem. Further, these past theories cannot be readily translated directly to physical applications since the necessary conditions for the transition from a single contact point to an extended contact region are not predicted. The gap between theory and physical systems calls for controlled experiments and the development of self-consistent models, which can accurately predict measurements.

Here, we combine precision model experiments, numerical simulations, and theoretical analyses to investigate the mechanical behavior of a three-dimensional (3D) homogeneous elastic rod wrapped around a rigid cylinder. Specifically, we aim at quantifying the effect of the finite bending stiffness and thickness of the rod on both the equilibrium geometry and the load transmission along the rod. Since the contact geometry plays an crucial role in dictating the mechanics of the system, we will first consider the simpler *static* case, where the rod is loaded by two equal loads at both extremities and therefore does not slide at the surface of the cylinder. In this frictionless configuration, we will show that numerical simulations based on the finite element method (FEM) reproduce the

experimental system accurately. Further, we will verify the possibility of presence of concentrated forces at the locations of touch-down and lift-off, as suggested by Stuart (1961). Next, in a second set of physical and numerical experiments, we will investigate the *sliding* case, where the rod is forced to slide continuously, in frictional contact at the surface of the cylinder. Both in the static and the sliding cases, we will leverage our observations of the experimental and numerical results to derive a model based on the theory of Euler's elastica. This model provides quantitative predictions of the mechanical behavior of our system at a much lower computational cost than required with the FEM, while also offering valuable physical insight of the underlying mechanisms. Building up on the work of Stuart (1961) and Jung et al. (2004, 2008b), our model includes the unknown contact geometry and the potential concentrated loads at the locations of touch-down and lift-off. The predictions from this model, with no adjustable parameters, will be compared to the experimental and numerical results, toward identifying their range of validity for practical applications. To the best of our knowledge, this study is the first to propose a direct comparison between the experimental, numerical and theoretical force transmission of an elastic rod of finite thickness in frictional contact with a rigid cylinder.

Our paper is organized as follows. First, in Section 2, we define the problem, in both the static and sliding configurations. Then, in Section 3, we detail the experimental and numerical methodology that we followed to quantify the mechanics of the 3D homogeneous elastic rod. In Section 4, we describe the 2D Euler's elastica theory. Next, in Section 5 and Section 6, we present the results of the static and sliding cases, respectively, comparing the experimental and numerical results with theoretical predictions. To highlight the relevance of the proposed framework to engineering applications, in Section 7, we show that the load transmission along commercially available belts used for power transmission can be accurately predicted by our theory. Finally, in Section 8, we will summarize and discuss our main findings.

2. Definition of the problem

In Fig. 1, we present photographs of the system we set out to investigate: an elastic rod wrapped around a rigid cylinder and loaded at its extremities by the vertical forces $\mathbf{F}_0 = -F_0\,\mathbf{e_y}$ and $\mathbf{F}_L = -F_L\,\mathbf{e_y}$. Ultimately, we are interested in rationalizing the role of friction on the equilibrium of the rod. As such, we build up complexity gradually by first focusing on the frictionless *static case* (Fig. 1A) and the move on to the frictional *sliding case* (Fig. 1B). In the static case, the loading forces are equal, $F_0 = F_L$, and induce no relative motion between the rod and the cylinder. In the sliding case, one extremity of the rod is weighted by the loading force, F_0, while a driving force, $F_L > F_0$, is applied at the other extremity to induce the motion of the rod at a constant velocity, U. Leveraging precision experiments and numerical simulations, we aim to characterize the geometry of the contact region and the load transmission along the rod under these external loads.

In our system, unlike the ideal filaments of the classic capstan problem, the rod has a finite bending stiffness and non-vanishing cross-sectional dimensions. We consider an elastomeric rod of length L, with a square cross-section of equal sides $H = W$, and a bending stiffness EI, where E is the Young's Modulus and $I = WH^3/12$ is the second moment of area. We restrict our study to planar deformations; the centerline of the rod is contained in a plane orthogonal to the cylinder axis (xy-plane). The square cross-section was, therefore, chosen to minimize out-of-plane displacements during experiments. The rigid cylinder of diameter D is clamped horizontally, with its axis aligned along $\mathbf{e_z}$. In the static case, we neglect frictional interactions, whereas in the sliding case, the rod-cylinder contact is characterized by a kinematic Amontons–Coulomb friction coefficient, μ.

In parallel to the experiments, we also carried out numerical simulations using the FEM on an equivalent system. Upon a thorough experimental validation, these FEM simulations enabled the precise reproduction of the rod-cylinder system over a wide range of loading conditions. Moreover, we used FEM simulations to quantify internal variables not accessible experimentally, such as the distributed contact pressure applied by the cylinder onto the rod or the internal forces along the rod, thus enabling thorough comparisons with the theoretical results.

Although we used the same experimental and numerical tools to study both the static and sliding cases, the quantities of interest in each of them differ. In the static case, we seek to relate the *total* wrapping angle, $\Delta\alpha_\text{tot}$ (defined by the angular extent of the contact region) to the loading forces $F_0 = F_L$. Based on FEM, we also study the *reduced* wrapping angle, $\Delta\alpha_\text{red}$ defined by the angle between the two peaks of the distributed contact force applied by the cylinder onto the rod. In the sliding case, we will quantify the driving-to-loading force ratio F_L/F_0, as a function of the loading force, F_0. We regard this quantity as representative of more complex and realistic systems such as engineering belts driven by motor pulleys, the tightening of knots or the mechanical behavior of fabrics.

To rationalize our findings, we will make use of the theory for planar Kirchhoff rods (i.e., Euler's elastica) and specialize it to our physical setup. Within this well-established theoretical framework, the shape of the rod is reduced to the position of its centerline $\mathbf{R}(S) = [X(S), Y(S), 0]$ along the arclength, S ($0 \le S \le L$). The mechanics of the rod is then dictated by kinematic and equilibrium conditions along the rod. Unlike previous modeling efforts of elastic rods on rigid cylinders, we will assume that the wrapping angle is an *unknown* of the problem that must be computed in either the static or the sliding cases. The proposed theory presented in Sections 4.2 and 4.3 is closed and self-consistent (with no adjustable parameters) and will enable a direct comparison with the experimental measurements and the numerical simulations.

3. Methods: Experiments and numerical simulations

To study the mechanical behavior of the generalized capstan problem, we performed precision physical experiments and numerical simulations based on the FEM. We investigated the contact mechanics both in the *absence* and in the *presence* of frictional sliding, respectively referred to as the *static* and *sliding* cases. In the *static case*, the two rod extremities were loaded quasi-statically
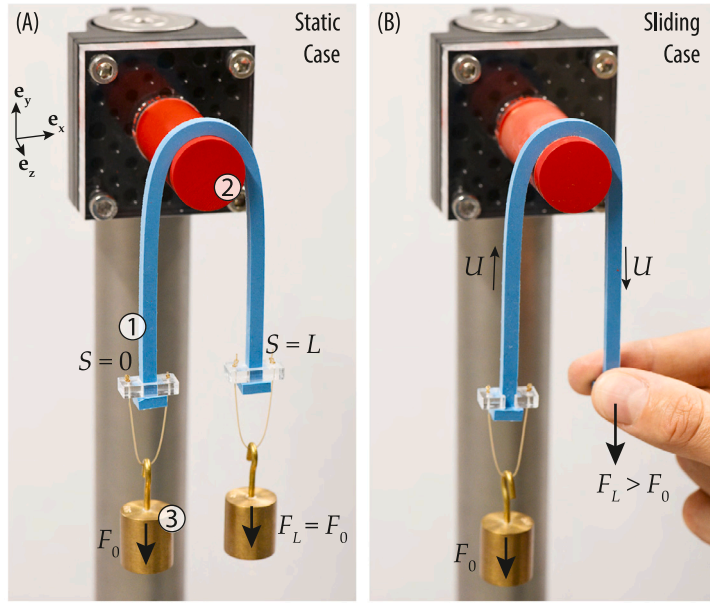
Fig. 1. An elastomeric rod wrapped around a cylinder. (A) In the static case, the elastic rod (1) is wrapped around a rigid cylinder (2) and weighted by two dead loads $F_0 = F_L$ (3) at each extremity. (B) In the sliding case, one extremity is weighted by a dead load, F_0, while a driving force, F_L, is applied at the other extremity to induce a continuous sliding motion of the rod at velocity U.

by two equal loads, thus yielding no rod-on-cylinder sliding. In the *sliding case*, a relative displacement was imposed continuously between the rod and the cylinder. In this section, we detail the methods employed to perform the physical experiments and numerical simulations. First, in Section 3.1, we describe the experimental fabrication methods (Section 3.1.1), apparatus (Section 3.1.2), and protocols (Section 3.1.3). Then, in Section 3.2, we present the FEM procedures used to numerically simulate and analyze the equilibrium configuration of the rod.

3.1. Experimental methods

3.1.1. Fabrication and characterization of rods and cylinders

We fabricated the elastic rods and the rigid cylinders with full control of their geometrical, mechanical, and contact properties. By contrast, the engineering belts studied in Section 7, in the context of power transmission applications, were purchased commercially but we characterized their geometric and mechanical properties thoroughly. Importantly, an experimental setup was designed to measure the rod-cylinder kinematic friction coefficient precisely. The fabrication and characterization procedures are presented next.

Rod Fabrication: Elastomeric rods were cast in-house out of vinyl poly-siloxane VPS32 (Elite Double 32, Zhermack), a silicone-based elastomer. Past studies (Baek et al., 2020; Grandgeorge et al., 2021; Johanns et al., 2021) have shown that the constitutive behavior of VPS32 is well approximated, up to stretches of 1.30, by an incompressible Neo-Hookean model with Young's modulus $E = 1.22 \pm 0.05$ MPa and Poisson's ratio $\nu \approx 0.5$. The rods were cast in a mold yielding a square cross-section of side $H = W = 5.0 \pm 0.1$ mm and a rod length $L = 200.0 \pm 0.1$ mm. To connect the rod extremities to either the load cell or loading masses, two thin square VPS32 pads (of side length 10 mm) were glued at the ends of the rod using a silicone adhesive (Sil Poxy, Smooth On). The total weight of the elastomeric rod and its end pads was 8.2 g.

To ensure reproducibility of the experimental measurements on the elastomeric VPS32 rods, in either the static or the sliding cases, particular attention had to be given to the following additional steps. For the static case, the rod was systematically cleaned (rinsed with water and dried off) to ensure the absence dust particles on its surface, so as to enable precise image analysis (described in Section 3.1.3). For the sliding experiments, we controlled the rod-cylinder frictional interaction by covering the elastomeric rod in talcum powder (Millette, Migros) for more than 24 h prior to the experimental measurements. After this time of surface treatment, the surface of the rod was wiped with a micro-fiber cloth covered in talcum powder before each experimental run. The details of the characterization of the kinematic friction coefficient are provided below. Still in the sliding case, in addition to the experiments performed with VPS32 rods, we also measured the load transmission along two commercial belts sliding in frictional contact with a steel cylinder. The first was a spring-steel conveyor belt of rectangular cross-section (thickness $H = 0.20$ mm and width $W = 9.95$ mm), and total length $L = 696$ mm (Misumi, ref: STHBLT0.2-10-2). The Young's modulus of this belt, $E = 155.8 \pm 2.5$ GPa, was determined from the linear regime of the stress–strain curve of a tensile test. No surface treatment was applied to the spring-steel belt. The second belt was a homogeneous polyurethane rod of circular cross-section (diameter $H = 5.95$ mm), length $L = 587$ mm and Young's Modulus $E = 22.1 \pm 1.9$ MPa (Misumi, ref: MBT6-600). To ensure a reproducible frictional behavior, the polyurethane
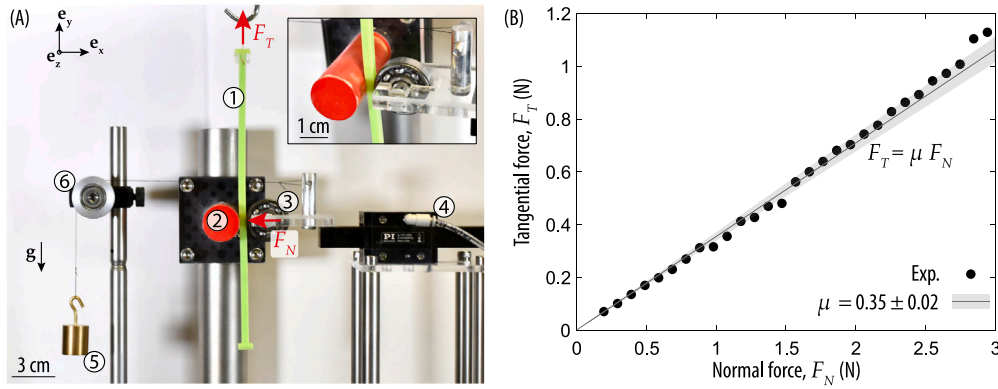
Fig. 2. Characterization of the kinematic friction coefficient between the rod and cylinder. (A) Photograph of the experimental setup. The elastomeric rod (1) is subjected to a normal load against the rigid cylinder (2) using a ball bearing (3) mounted on a linear air-bearing (4). The normal load is induced by a calibrated mass (5) and oriented horizontally using a pulley (6). (B) Stationary tangential force, F_T, driving the continuous upward displacement of the rod as a function of the normal load (experimental data points). The linear fit and the corresponding confidence interval are represented by the solid line and shaded region.

rod was wiped with the degreasing agent WD-40 (Distrelec, Switzerland) and subsequently covered in talcum powder prior to each experimental run.

Cylinder Fabrication: For the experiments performed with the VPS32 rods, we used prefabricated Polyoxymethylene cylinders (Misumi, Young's modulus ≈ 3 GPa) with four different diameters, D={5, 10, 25, 50}±0.1 mm, and axial lengths between 20 and 40 mm. The cylinders were spray-painted red (red platinum, dupli-color, Motip Dupli) to increase contrast with the elastomeric rod. For the static case, this enhanced contrast was necessary for the automated image analysis performed to quantify the total wrapping angle (see Section 3.1.3). For the sliding experiment, we controlled the rod-cylinder frictional behavior by replicating the rod surface treatment on the rigid cylinder. The cylinders were first coated with a thin layer of VPS32 using a technique based on Landau–Levich dip coating (Landau and Levich, 1988). We poured still-liquid VPS32 elastomer on the cylinder and then placed it in an upright position, thus enabling the elastomer to drain under gravity before curing. Once cured, the resulting layer of solid VPS32 (thickness < 0.1 mm) was surface-treated with talcum powder following the same protocol as described above for the elastomeric rod. For the experiments performed on the commercial spring-steel and polyurethane belts, we used a polished stainless steel cylinder of diameter $D = 50$ mm (Misumi, part number PSTS50-200), with no surface treatment.

Characterization of the Kinematic Friction Coefficient: In Fig. 2A, we present a photograph of the apparatus designed to characterize the rod-cylinder kinematic friction coefficient *in situ*. The upper extremity of the rod was attached to a 1-kN load cell of the mechanical testing machine (Instron 5943). Next, the rod was pressed against the rigid cylinder with a controlled normal load, F_N, using an annular ball bearing (of external diameter 30 mm) loaded using a calibrated mass–pulley system; see (3), (4), (5), and (6) in Fig. 2A. We imposed normal loads in the range $1.96 \leq F_N$ [N] ≤ 29.4 by gradually hanging a set of masses of 10 g. Under this normal load and the resulting frictional interaction with the cylinder, the upper extremity of the rod was pulled upward at a constant velocity, $U = 3$ mm/s, and the stationary pulling force, F_T, was monitored. Note that the value of U was chosen equal to the displacement velocity imposed in the experiments of the sliding case.

In Fig. 2B, the experimental data of F_T versus F_N are plotted along with the corresponding linear fit $F_T = \mu F_N$ for the surface-treated VPS32 rods on a cylinder of diameter $D = 25$ mm. The kinematic friction coefficient was determined from F_T/F_N to be $\mu = 0.35 \pm 0.02$, in close agreement with values reported in the literature for similar fabrication and talcum-based coating techniques on vinyl poly-siloxane polymers (Baek et al., 2020; Grandgeorge et al., 2021). The robustness and reproducibility of μ, together with the validity of the classic Amontons–Coulomb friction law over a wide range of normal loads, were essential to enable the direct comparison between the experiments, simulations, and theory. Using the same setup, we measured the kinematic friction coefficient of the commercial spring-steel and polyurethane belts on the steel cylinder to be $\mu = 0.15 \pm 0.1$ and $\mu = 0.26 \pm 0.2$, respectively.

3.1.2. Experimental apparatus

Performing experiments on either the static or the sliding cases required developing two distinct specialized apparatus, both of which are described next.

Static Case: In Fig. 3A, we present the experimental setup designed to measure the total wrapping angle in the static case. The rigid cylinder was clamped horizontally (along $\mathbf{e_z}$) to an acrylic plate mounted vertically, and the elastomeric rod was placed on the cylinder near its free end, ensuring that the side of the rod facing the camera was aligned with the flat face of the cylinder. We imaged the rod-on-cylinder system with a Nikon D850 camera (lens Sigma Apo Macro DG HSM 150 mm f2.8) in the presence of a white backlight, to enhance the contrast between regions of rod-cylinder contact and regions of no contact. Parallax artifacts were
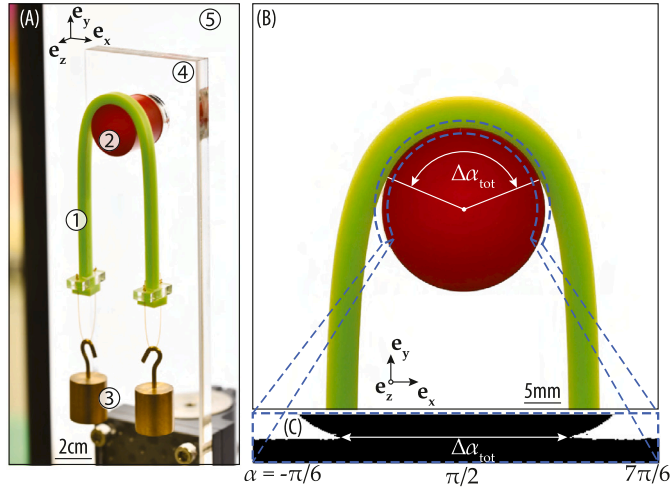
Fig. 3. Experimental setup of the static case used to measure the total wrapping angle, $\Delta\alpha_{tot}$. (A) The elastomeric rod (1) is wrapped around the rigid cylinder (2) and weighted by two equal dead loads (3). In this representative example, $F_0 = 0.98$ N. The rigid cylinder is clamped to an acrylic plate (4), and the system is back-illuminated using a planar light source (5). (B) Representative photograph of the rod-on-cylinder system. The boundaries of the contact region are extracted using an automated image analysis algorithm based on brightness differences, yielding the binarized annular portion of the photograph presented in panel (C).
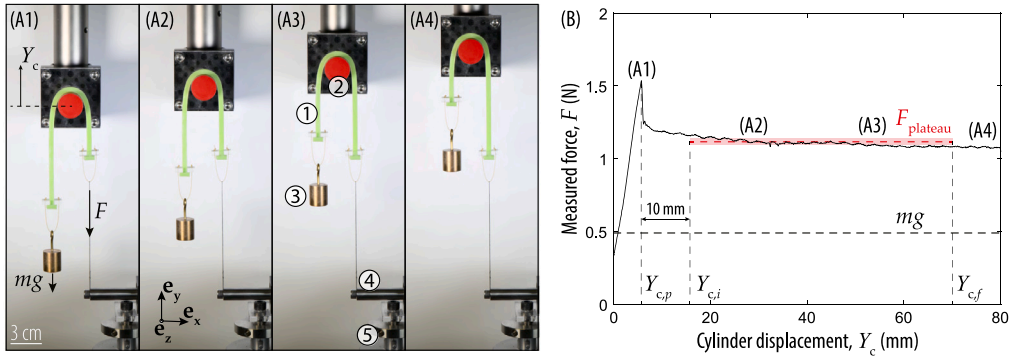

Fig. 4. Experimental setup of the sliding case used to measure the driving-to-loading force ratio. (A) Series of photographs obtained during an experiment. The rod (1) is suspended from the cylinder (2) and weighted with a vertical loading force $\mathbf{F_0} = -F_0\mathbf{e_y}$ (3) at its left extremity. The right extremity is attached to the shaft of a linear air-bearing (4), allowing for the free horizontal motion of the rod extremity in the x-direction while constraining its position in the y-direction. The reaction force $\mathbf{F} = -F\mathbf{e_y}$ holding the right rod extremity during the upward displacement of the cylinder (Y_c) is monitored by the load cell (5) on which the linear air-bearing shaft is fixed. (B) Representative force–displacement curve for a loading mass of $m = 50$ g (*i.e.*, to $F_0 = mg = 0.49$ N). The dashed line corresponds to $F_{plateau}$, the average value of F in the region of Y_c ranging from an initial displacement $Y_{c,i}$ up to $Y_{c,f} = 70$ mm. The shaded area around $F_{plateau}$ shows the standard deviation of the force signal in $Y_{c,i} \leq Y_c \leq Y_{c,f}$.

minimized by positioning the camera far from the rod-cylinder system, at a distance $\mathcal{L} = 40D$. A typical photograph used for image analysis is provided in Fig. 3B.

Sliding Case: In Fig. 4A, we present the experimental setup designed to measure the driving-to-loading force ratio in when a continuous displacement is imposed between the rod and the cylinder. One extremity of the rod was weighted by a vertical loading force (hanging mass), and the other one was attached to a 1-kN load-cell through a horizontal linear air-bearing. This air-bearing fixed the vertical y-position of the right extremity of the rod while allowing for a free horizontal x-displacement. Finally, to induce sliding, the rigid cylinder was displaced upward, and the force applied at the right end of the rod was monitored throughout this displacement.

3.1.3. Experimental protocols

We proceed by describing the experimental protocols. First, we detail the image analysis algorithm used to quantify the total wrapping angle in the static case. Then, we focus on the measurement of the driving-to-loading force ratio of the sliding case.

Static Case: The rod was loaded by two identical masses at both its extremities, imposing a loading force ranging from $F_0 = 0.98$ N to 31.4 N, with an incremental step of 0.98 N by sequentially adding masses of 10 g. At each step, the total wrapping angle was extracted by analyzing the photograph with an automated algorithm coded in-house (Matlab 2019b, Mathworks). The image was first

binarized based on brightness and a circular strip of the image centered around the cylinder axis was extracted in polar coordinates (see blue dashed lines in Fig. 3B). Finally, from this flattened strip, the total wrapping angle, $\Delta\alpha_{\mathrm{tot}}$, was extracted based on the total extent of the contact region, as shown in Fig. 3C, where the dashed bounding box corresponds to the dashed lines in Fig. 3B.

Due to perspective in the photograph, the parallax effect induced a small uncertainty when quantifying $\Delta\alpha_{\mathrm{tot}}$. To control this artifact, the camera was placed sufficiently far (at a distance $\mathcal{L} = 40D$) from the rod-cylinder system to increase the parallelism of the incoming light rays. The effect of this parallax artifact is characterized by a minimal gap between the rod and the cylinder, δ_{min}, that enables light transmission from the backlight. Using the intercept theorem, we find $\delta_{\mathrm{min}} = W(D/2)/\mathcal{L} = 62.5$ μm. Therefore, the contact-free region where the rod is closer than 62.5 μm from the surface of the cylinder is attributed to contact. This controlled experimental uncertainty was accounted for when validating the FEM computations against experiments, as detailed in Section 3.2.

Sliding Case: In this set of experiments, only the left extremity of the rod was loaded by a calibrated mass, imposing a loading force ranging from 0.98 N to 31.4 N with an incremental step of 0.98 N, while the right extremity was fixed at a constant height. As described in Section 3.1.2, the sliding motion between rod and cylinder was induced by the upward displacement of the rigid cylinder. The vertical force, F, required to fix the height of the right extremity, was monitored throughout the cylinder displacement. The constant displacement velocity, U, was chosen to be small ($U = 3$ mm/s) to minimize the influence of inertial effects on the force–displacement response. Indeed, the characteristic distributed centrifugal acceleration force in the curved rod-cylinder contact region is $F_a = 2\rho H^2 U^2/(D + H)$ and the contact forces scale as $F_c \sim 2F/(D + H)$. Hence, $F_a/F_c \sim 10^{-7}$ using $\rho = 1200$ kg/m³ for the VPS density, and a characteristic loading force of $F = 1$ N, thus confirming that inertial effects can be neglected.

In Fig. 4B, we present a representative force–displacement curve of a sliding experiment. The force signal first increases with cylinder displacement, Y_c, up to a peak value at $Y_{c,p}$, after which the force drops to an approximately constant value, F_{plateau}. The slight decay within the measured plateau is attributed to the variation of the self-weight of the loaded (left) strand of the rod throughout displacement. As the rigid cylinder is pulled upward, the length of this left strand decreases, and, therefore, its effective weight decays, inducing a gradual reduction in the measured force. Despite this small decay, we determined F_{plateau} as the average value of F measured from the displacement $Y_{c,i} = Y_{c,p} + 10$ mm to $Y_{c,f} = 70$ mm (dashed red line in Fig. 4B) with an uncertainty defined as the standard deviation of the force signal over the same displacement range (shaded red area). Finally, we introduced a small correction to account for the contribution of the rod self-weight to the imposed and measured forces. We took the approximation that half of the total rod weight was concentrated at each rod extremity, thus modifying the actual loading and driving forces: $F_0 = Mg + F_{\mathrm{rod}}/2$ and $F_L = F_{\mathrm{plateau}} + F_{\mathrm{rod}}/2$, with $F_{\mathrm{rod}} = 0.08$ N. This correction was particularly important for the smaller loading forces where the relative weight of the rod was non-negligible. Using this protocol, we characterized the driving-to-loading force ratio, F_L/F_0, as a function of the loading force, F_0, for the rigid cylinder diameters $D = 5, 10, 25$, and 50 mm.

3.2. Finite element simulations

We employed the finite element method (FEM) to simulate the 3D elastic rod on a rigid cylinder. Using the `STATIC,GENERAL` solver of the commercial package software ABAQUS-STANDARD (Simulia, Dassault Systèmes), we simulated a rod-cylinder system equivalent to its experimental counterpart by reproducing the geometry and mechanical properties of the physical elastic rods in a dimensionless framework. Lengths were defined in units of rod thickness, and forces were defined in units of EA, the characteristic axial force of the rod (where E and A are the dimensional Young's Modulus and the cross-sectional area of the rod, respectively). In this section, unless stated otherwise, all quantities are expressed in their dimensionless form (lower-case letters). As discussed in Section 3.1.3, inertial effects can be reasonably neglected in both the static and sliding cases. Therefore, we assumed that the elastic rod had zero mass. Upon detailed validation with experiments, the simulations enabled us to probe quantities not readily accessible in experiments, such as the distributed contact pressure at the cylinder surface or the internal forces in the elastic rod. We now provide details on the protocols and post-processing steps of our numerical computations.

3.2.1. Numerical protocols

The rod was constructed with a rectangular cross-section of unit thickness $h = 1$ and length $\ell = 40$. Taking advantage of the in-depth symmetry about the $x - y$ plane, we only simulated one half the system, setting the width of the half-rod to 0.5. Further, we defined the material centerline of the rod as its longitudinal mid-axis at rest, and the undeformed arclength, s, was defined along this centerline (with $0 \leq s \leq \ell$). The rigid cylinders were generated with dimensionless diameters $d = 1, 2, 5$, and 10.

The rod was meshed using 3D hexahedral elements with reduced integration and hybrid formulation (C3D8RH), with an incompressible Neo-Hookean hyperelastic material model of unit (dimensionless) Young's modulus. The mesh density of the elastic rod necessary for convergence depended on the diameter of the rigid cylinder, d. Smaller diameters induce larger curvatures and, therefore, require a finer mesh density to accurately compute the larger strains of the bent rod. Therefore, the mesh of the rod was refined near the contact region depending on the cylinder diameter. In a region centered around the mid-point $(\ell/2 - 3d) \leq s \leq (\ell/2 + 3d)$, the mesh density was set to $100/d$ elements per unit length. Outside this refined region, the mesh density was set to 10 elements per unit arclength. The cylinder was meshed using the Abaqus discrete rigid surface mesh with a density of $200/d$ elements per unit length. As the only exception, the mesh densities of the configuration with $d = 1$ had to be decreased to $50/d$ and $100/d$ elements per unit length for the finely-meshed part of the rod and the cylinder surface, respectively, to reduce the total number of nodes, thus avoiding saturation of the computer memory.

The loading steps of the rod in the FEM simulations differed slightly from the physical experiments. In FEM, both for the static and sliding cases, the rod was loaded by imposing two equal vertical displacements to both extremities with incremental steps of dimensionless position $\Delta y = 0.05$, yielding approximately 100 loading steps for each simulated configuration. To reproduce the
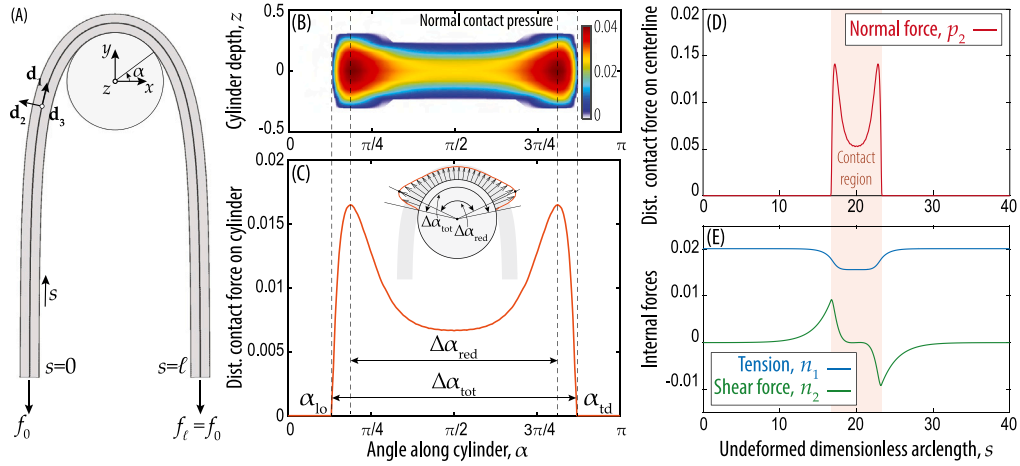
Fig. 5. Representative examples of the profiles of the external and internal forces along the rod arclength, for the static case for $d = 5$ and $f_0 = 2 \times 10^{-2}$. (A) Snapshot of the FEM computation. (B) Normal contact pressure map at the cylinder surface (the pressure is normalized by EA/H^2). (C) Integrated contact pressure, yielding the distributed contact force at the surface of the cylinder, per unit circumferential length. Inset: schematic representation of the distributed contact force (solid orange line) and the total and reduced wrapping angle, $\Delta\alpha_{tot}$ and $\Delta\alpha_{red}$, respectively. (D) Normal distributed contact force, p_2 (per unit undeformed arclength of the rod). (E) Profiles of the tension and shear components of the internal force, **n**. The contact region is highlighted in orange in panels (D) and (E).

purely vertical end forces applied in the experiments, both extremities were unconstrained in the horizontal x-direction. In the static case, the contact between the surface of the rod and the rigid cylinder was governed by the frictionless *PENALTY* interaction. In the sliding case, the rigid cylinder was set to rotate anti-clockwise (2 radians) between each displacement step, thereby inducing the relative displacement between rod and cylinder. Given the experimentally-measured kinematic friction coefficient of $\mu = 0.35 \pm 0.02$, we performed the sliding computations with $\mu = \{0.33, 0.35, 0.37\}$, so as to represent the 68% confidence interval of experimental data.

3.2.2. Extraction of the distributed contact force and the internal force profiles

We leveraged the simulations to extract the distributed contact force applied by the cylinder onto the rod, as well as the resulting profile of internal force along the rod. In Fig. 5, we detail the post-processing procedure employed to compute these force profiles. Note that, for brevity, we describe our protocol only for the static case, but the same steps were followed for the sliding case.

In Fig. 5A, we present a snapshot of FEM for a cylinder of diameter $d = 5$, at the loading force $f_0 = f_\ell = 2 \times 10^{-2}$. We defined a material local frame by the triad $\{\mathbf{d_1}, \mathbf{d_2}, \mathbf{d_3}\}$ adapted to the arclength, s. The unit vector, $\mathbf{d_1}$, is tangent to the deformed centerline, and the unit vectors, $\mathbf{d_2}$ and $\mathbf{d_3} = \mathbf{e_z}$ correspond to the normal and binormal vectors to $\mathbf{d_1}$, respectively. External and internal forces along the elastic rod will be projected onto this local frame with subscripts 1, 2 and 3 referring to the projections of a force along $\mathbf{d_1}$, $\mathbf{d_2}$ and $\mathbf{d_3}$.

In Fig. 5B, we provide an example of the distribution of the contact pressure at the surface of the cylinder. By integrating this 2D contact pressure along the depth of the cylinder surface, we first extracted the 1D distribution of the contact force along the angle, α, at the cylinder surface, as represented in Fig. 5C. Next, to enable comparisons with centerline-based theories, we expressed the contact force, **p**, in units of force per undeformed arclength of the centerline, an example of which is given in Fig. 5D. Finally, making use of **p**, we computed the internal force along the rod, $\mathbf{n} = n_1 \mathbf{d_1} + n_2 \mathbf{d_2}$. At mechanical equilibrium, the internal force at the kth node of the centerline, $\mathbf{n}(s_k)$, applied by the right strand of the rod ($s > s_k$) to the left strand ($s < s_k$) must satisfy

$$\mathbf{n}(s_k) + \mathbf{f_0} + \sum_{i=1}^{k} \mathbf{p}(i)\delta s_i = \mathbf{0}, \tag{2}$$

where $\delta s_i = s_{i+1} - s_i$, defined in the rod undeformed state (distance between two consecutive nodes of the material centerline). Finally, in Fig. 5E, we plot the tensile and shear components (n_1 and n_2) of the internal force along s. In Sections 5 and 6, we will show that these force profiles can be approximated well by Euler's elastica (presented in Section 4) in both the static and sliding cases.

3.2.3. Contact geometry and load transmission along the rod

In the static case, we leveraged FEM to quantify the extent of the contact region and the distribution of the contact force at the cylinder surface. Specifically, we extracted the *reduced* and *total* wrapping angles, $\Delta\alpha_{red}$ and $\Delta\alpha_{tot}$, both of which are represented schematically in the inset of Fig. 5C. The reduced wrapping angle is defined as the angle between the location of the two force peaks at the surface of the cylinder and the total wrapping angle corresponds to the complete angular extent of the contact region. Since α_{tot} was also measured experimentally, we used this quantity to validate our FEM simulations against experiments (see Section 5).
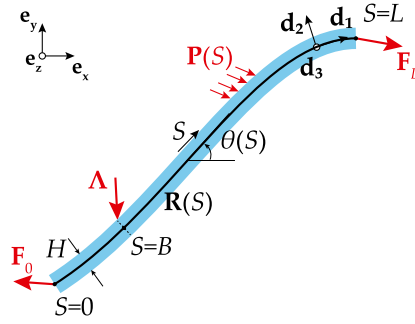
Fig. 6. Schematic diagram of an elastic rod under external loading in 2D. The rod is subjected to distributed and concentrated external forces at its surface, $\mathbf{P}(S)$ and $\mathbf{\Lambda}$, respectively.

In the sliding case, we computed the driving-to-loading force ratio, f_ℓ / f_0, over the wide range of loading forces, $10^{-3} \leq f_0 \leq 10^{-1}$. Experimentally, the range of loading forces was more restrictive, as the smallest experimental value of f_0 was 5×10^{-3}. The FEM simulations were validated against experiments by comparing the evolution of f_ℓ / f_0 versus f_0 as detailed in Section 6.

4. Theoretical description of the rod-cylinder contact mechanics

Theoretical models describing the mechanics of an elastic rod in contact with a rigid cylinder have been proposed in literature (Stuart, 1961; Jung et al., 2004, 2008a). In these studies, the authors assumed that the extent of the contact region (*i.e.*, the wrapping angle) was known *a priori*. In reality, the contact geometry is not a known control parameter as it results from the non-trivial interplay between geometry, bending stiffness, friction, and the load applied at the rod extremities. To provide a comparison between experiments, numerical simulations, and theory, we derived a complete theoretical framework to predict the wrapping angle and the internal load transmission along the rod. Our model is built on the classic Kirchhoff-rod theory in 2D, commonly referred to as Euler's elastica, to derive sets of ODEs, which we solved numerically under the relevant boundary and matching conditions using the Matlab function bvp5c (Mathworks, 2019). In Section 4.1, we will first review the equations governing the mechanics of the rod based on Euler's elastica. Then, in Section 4.2 we will specialize the equations to the static case to compute the shape of a rod in the absence of friction. Finally, in Section 4.3, we will derive a model for the sliding case, enabling the prediction of the driving-to-loading force ratio.

4.1. Review of the theory of Euler's elastica in the presence of distributed and concentrated forces at the rod surface

The classic Kirchhoff-rod model (Kirchhoff, 1859) is often used to predict the behavior of an elastic rod under external loads (Landau and Lifshitz, 1986; Dill, 1992; Audoly and Pomeau, 2010; Bigoni, 2015; Goriely, 2017). Within this framework, the rod is assumed to be slender, such that $L \gg H, W$, and the 3D mechanics can, therefore, be reduced to a 1D description of the rod geometry and its internal efforts along the arclength, $0 \leq S \leq L$, of its centerline. The rod, of bending stiffness EI, can undergo bending but is considered inextensible and unshearable, meaning that its centerline can neither stretch nor contract and that its cross-sections remain orthogonal to the centerline when the rod is deformed.

In this section, we review the well-established theory of the Euler's elastica, which we will employ to derive a set of ODEs governing the behavior of the rod when brought in contact with the rigid cylinder. We will especially focus on the effect of distributed and concentrated forces applied at the surface of the rod, as these loads can exert external torques to the centerline of the rod, thus playing a key role in dictating its overall mechanical response. In Section 3.1.3, we showed that inertial effects play a negligible role in the capstan experiments and, therefore, we do not account for dynamics in the present model, assuming that the rod is at static equilibrium.

In Fig. 6, we present a schematic diagram of a 2D elastic rod subjected to external forces. The rod is naturally straight at rest, and its extremities are loaded by the two forces $\mathbf{F}_0$ and $\mathbf{F}_L$. In addition, the rod is subjected to distributed contact and point contact forces, $\mathbf{P}(S)$ and $\mathbf{\Lambda}$, respectively, applied onto its surface. We now review the framework of Euler's elastica, considering the kinematics, the force and moment balance equations, and the jump conditions under concentrated loads.

Kinematics: The shape of the deformed elastic rod is represented by the position of its centerline $\mathbf{R}(S) = X(S)\mathbf{e_x} + Y(S)\mathbf{e_y}$. A local frame is defined by the tangent and normal vectors $\mathbf{d_1}(S) = \mathbf{R}'(S) = \cos\theta(S)\mathbf{e_x} + \sin\theta(S)\mathbf{e_y}$, $\mathbf{d_2}(S) = -\sin\theta(S)\mathbf{e_x} + \cos\theta(S)\mathbf{e_y}$, and $\mathbf{d_3} = \mathbf{e_z}$, where the angle $\theta(S)$ represents the angle between $\mathbf{d_1}$ and the horizontal axis, $\mathbf{e_x}$. In the inextensible case that we consider, the kinematic relations between the position of the centerline and the angle are

$$X'(S) = \cos\theta, \tag{3}$$

$$Y'(S) = \sin\theta, \tag{4}$$

where the angle $\theta(S)$ is related to the curvature, $K(S) = \theta'(S)$, of the rod centerline. Note that the prime notation, $[\cdot]'$, represents derivatives with respect to S.

Force and Moment Balance: The internal loads along the rod centerline are reduced to an internal force, $\mathbf{N}$, and an internal moment, $\mathbf{M}$, applied to the cross-section at S by the segment of the rod of $\overline{S} > S$. The moment–curvature constitutive relation of the rod is commonly described by

$$M(S) = EI\, K(S), \tag{5}$$

where the internal moment is $\mathbf{M} = M\mathbf{d_3}$. Next, under the equilibrium conditions of force and moment balance, the Euler's elastica equations are written as derived in (Landau and Lifshitz, 1986; Dill, 1992; Audoly and Pomeau, 2010; Bigoni, 2015; Goriely, 2017) :

$$\mathbf{N}'(S) + \mathbf{P}(S) = \mathbf{0} \tag{6}$$
$$\mathbf{M}'(S) + \mathbf{d_1}(S) \times \mathbf{N}(S) + \mathbf{Q}(S) = \mathbf{0}. \tag{7}$$

Note that the vectorial Eq. (6) corresponds to two scalar equations. The contact force $\mathbf{P} = P_1\mathbf{d_1} + P_2\mathbf{d_2}$ is an external distributed force (per a unit rod length), applied at the surface of the rod, *i.e.*, at a location $\mathbf{R} \pm H/2\,\mathbf{d_2}$. Under this distributed contact force, the rod centerline is subjected to the external distributed torque

$$\mathbf{Q} \equiv \left(\pm\frac{H}{2}\mathbf{d_2}\right) \times \mathbf{P} = \mp P_1\frac{H}{2}\mathbf{d_3}. \tag{8}$$

As detailed below in Section 4.2, this distributed torque plays an important role in setting the overall load transmission along an elastic rod in frictional contact with a rigid cylinder.

Eqs. (5)–(7), supplemented by the kinematic relations Eqs. (3) and (4), are the six classic scalar differential equations describing the mechanics of a rod subjected to external loads.

Jump Conditions under a Concentrated Contact Force: When an elastic rod is brought in contact with a surface, concentrated forces and moments may arise at the locations of touch-down and lift-off between the rod and the surface, as suggested by Stuart (1961). We now focus on the jump in the internal force and moment profiles along a rod subjected to a concentrated force applied onto its surface, as such a point load might induce a discontinuity of the internal forces $\mathbf{N}(S)$ and moments $\mathbf{M}(S)$ in the rod (Audoly and Pomeau, 2010). We investigate this effect by focusing on the contact force $\mathbf{\Lambda}$ applied at the rod surface at $S = B$, as presented schematically in Fig. 6. We consider the mechanical equilibrium of an infinitesimal rod element centered around B, within $B^- < S < B^+$, where

$$B^- \equiv \lim_{\omega \to 0}(B - \omega), \quad B^+ \equiv \lim_{\omega \to 0}(B + \omega), \tag{9}$$

and $\omega > 0$ is a small parameter. Balance of force on this infinitesimal element yields

$$\mathbf{N}(B^+) = \mathbf{N}(B^-) - \mathbf{\Lambda}, \tag{10}$$

revealing the jump in the rod internal force at $S = B$.

In addition to the jump of internal force expressed in Eq. (10), the external contact concentrated force $\mathbf{\Lambda} = \Lambda_1\mathbf{d_1}(B) + \Lambda_2\mathbf{d_2}(B)$ also induces a jump in the internal moment. When $\mathbf{\Lambda}$ is applied at the rod-surface $\mathbf{R}(B) \pm (H/2)\mathbf{d_2}(B)$, the centerline of the rod is subjected to the contact torque

$$\mathbf{\Psi} \equiv \left(\pm\frac{H}{2}\mathbf{d_2}\right) \times \mathbf{\Lambda} = \mp\Lambda_1\frac{H}{2}\mathbf{d_3}. \tag{11}$$

Considering the moment balance of the infinitesimal rod element, the concentrated torque $\mathbf{\Psi}$ induces the internal moment discontinuity

$$\mathbf{M}(B^+) = \mathbf{M}(B^-) - \mathbf{\Psi}. \tag{12}$$

When specializing the elastica equations to the rod-cylinder system, the discontinuities of Eqs. (10) and (12) will be essential to express the matching conditions at the touch-down and lift-off locations, as detailed in Sections 4.2 and 4.3 for the static and sliding cases, respectively.

Dimensionless Formulation of the Elastica Equations: We now write the dimensionless elastica equations by normalizing lengths by the thickness of the rod, H, and forces the characteristic axial force EA. Similarly to the FEM framework described in Section 3.2, lower cases will refer to the dimensionless variables corresponding to the capitalized dimensional quantities:

$$(s, x, y, z, \ell, d) = \frac{(S, X, Y, Z, L, D)}{H}, \quad (\mathbf{n}, \lambda, \mathbf{f_0}, \mathbf{f_\ell}) = \frac{(\mathbf{N}, \mathbf{\Lambda}, \mathbf{F_0}, \mathbf{F_L})}{EA},$$

$$\kappa = KH, \quad \mathbf{p} = \frac{\mathbf{P}H}{EA}, \quad (\mathbf{m}, \boldsymbol{\psi}, m) = \frac{(\mathbf{M}, \mathbf{\Psi}, M)}{EAH}, \quad (\mathbf{q}, q) = \frac{(\mathbf{Q}, Q)}{EA}.$$

The elastica equations reviewed previously, Eq. (3) to Eq. (7), are then rewritten as

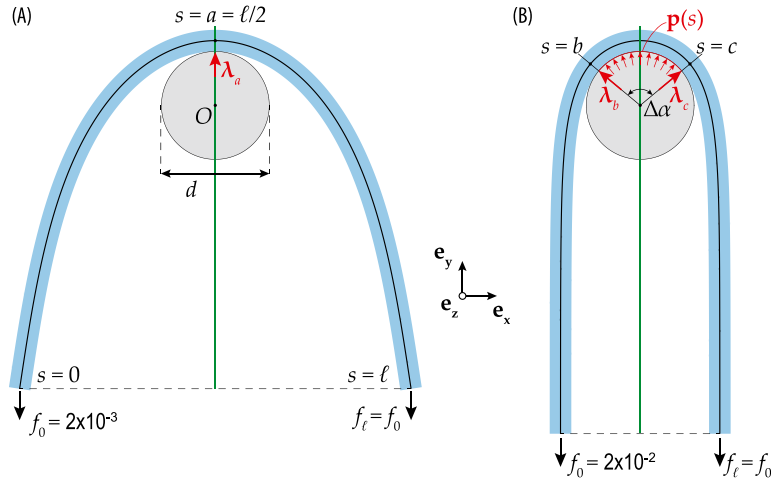$$x'(s) = \cos\theta(s), \tag{13}$$
$$y'(s) = \sin\theta(s), \tag{14}$$

Fig. 7. Schematic representation of the static case in the small and large-loading regimes. **(A)** Small-loading regime. At $f_0 = 2 \times 10^{-3}$, the rod shares one contact point with the cylinder at arclength $s = a = \ell/2$. At this contact location, the cylinder applies a concentrated force, λ_a. **(B)** Large-loading static regime. At $f_0 = 2 \times 10^{-2}$, the contact region is characterized by an extended contact line ranging from arclength $s = b$ to $s = c$ (with the symmetry condition $\ell/2 - b = c - \ell/2$). The cylinder applies the forces λ_b and λ_c at $s = b$ and $s = c$ and a distributed normal contact force $\mathbf{p}(s)$ between these two locations. The unknown wrapping angle, $\Delta\alpha$, characterizes the extent of the contact region.

$$\mathbf{n}'(s) + \mathbf{p}(s) = \mathbf{0}, \tag{15}$$

$$\mathbf{m}'(s) + \mathbf{d_1}(s) \times \mathbf{n}(s) + \mathbf{q}(s) = \mathbf{0}, \tag{16}$$

$$m(s) = \xi\theta'(s). \tag{17}$$

The geometric parameter $\xi = I/AH^2$ appearing in Eq. (17) can be interpreted as a normalized bending stiffness of the rod, representing the ratio between the characteristic bending force EI/H^2 and the characteristic axial force of the rod EA. This parameter depends solely on the shape of the rod cross-section. For example, $\xi = 1/12$ in the case of a rectangular cross-section (of thickness H), and $\xi = 1/16$ for a cylindrical elastic rod (of diameter H).

Finally, the dimensionless jump conditions at $s = b$ corresponding to Eqs. (10) and (12) are

$$\mathbf{n}(b^+) - \mathbf{n}(b^-) + \lambda = \mathbf{0} \tag{18}$$

$$\mathbf{m}(b^+) - \mathbf{m}(b^-) + \psi = \mathbf{0}. \tag{19}$$

The classic elastica model detailed above yields a set of six scalar ODEs, given by Eqs. (13) to (17), which are supplemented by the jump conditions of internal force and moment described by Eqs. (18) and (19), to model the present problem of rod wrapped on a cylinder. In Sections 5 and 6, we will show that, for large enough dimensionless cylinder diameters ($d \gtrsim 5$), the ODE-based theoretical framework provides excellent predictions for the extent of the contact region and load transmission along the elastic rod, at a computational cost significantly lower than full-3D FEM simulations.

4.2. Static frictionless case

We now specialize the general model presented in the previous section to the static case, when the rod and the cylinder interact without friction. To mimic the experiments, the extremities of the rod are weighted by two equal loading forces $f_0 = f_\ell$. In Fig. 7, we present two schematics of our system at the loading forces $f_0 = f_\ell = 2 \times 10^{-3}$ (A) and 2×10^{-2} (B). Since the system is symmetric with respect to the y-axis, we will only model the left half of the rod ($0 \le s < \ell/2$) to minimize the computational cost of integrating the resulting ODEs.

In experiments and FEM, we observed that the nature of the contact between the rod and the cylinder transitions from a small localized region to an extended area as the loading force f_0 is increased (see results in Section 5). This transition was also proposed by Stuart (1961). In the theoretical model, we will, therefore, assume that contact is characterized by single contact point (at $s = a = \ell/2$) at small values of f_0, and by an extended contact line ranging from $s = b$ to $s = c$ for larger values of f_0, as presented schematically in Fig. 7A and Fig. 7B, respectively. Note that in the case of the extended contact line, we only consider a continuous contact, as discontinuities of the contact region were not observed, neither in the experiments, nor in the numerical simulations. The theoretical model will further enable us to predict critical loading force $f_0^\star$, at which the contact region transitions from a single point to an extended line. In addition, the model will also describe the wrapping angle and the profiles of external and internal forces along the rod. In Section 4.2.1, we derive a complete set of ODEs corresponding to the case of single contact point (referred to as the *small-loading static regime*). Then, in Section 4.2.2, an analogous derivation will yield ODEs in the case of an extended contact line (referred to as the *large-loading static regime*).

4.2.1. Small -loading static regime: a single contact point

For small values of f_0, the contact between the elastic rod and the rigid cylinder is assumed to be limited to a single contact point. At the contact location, $s = a = \ell/2$, the cylinder applies a concentrated force λ_a and the rod is free of contact forces in $0 \leq s < \ell/2$. The rod mechanics in this region are, therefore, governed by the six scalar elastica equations of Eqs. (13)–(17), in the absence of external loads, such that $\mathbf{p} = \mathbf{q} = \mathbf{0}$, together with the appropriate boundary conditions at $s = 0$ and $s = \ell/2$:

$$n_x(0) = 0 \qquad n_y(0) = f_0, \qquad m(0) = 0 \tag{20}$$

and

$$x(\ell/2) = 0 \qquad y(\ell/2) = \frac{1+d}{2}, \qquad \theta(\ell/2) = 0. \tag{21}$$

We integrated the set of elastica equations with the six boundary conditions provided in Eqs. (20) and (21) for increasing values of the loading force, f_0. At each step, we monitored the curvature profile of the centerline whose maximum (absolute) value was systematically observed at the location of contact, $s = a = \ell/2$. We characterized the transition between the single contact point and the extended contact line by the value of $f_0^\star$ for which the curvature $\kappa(s = \ell/2)$ reached the critical curvature of a rod fully wrapped around the cylinder, $\kappa^\star = -2/(1+d)$. Beyond this critical point, for $f_0 > f_0^\star$, the single contact model yielded a non-physical penetration of the rod into the cylinder. The emergence of an extended contact line was accounted for in the large-loading static regime, presented next.

4.2.2. Large -loading static regime: an extended contact line

We now focus on the case of an extended contact line. The rod initiates contact with the cylinder at the unknown touch-down location, $s = b$, and the lift-off location, $s = c$ is given by the symmetry condition: $\ell/2 - b = c - \ell/2$. The contact geometry is characterized by the unknown wrapping angle, $\Delta\alpha$, as sketched in Fig. 7B. To compute the two unknowns, b and $\Delta\alpha$, for varying loading force, $f_0 > f_0^\star$, we solved the rod equations in the contact-free region of the rod ($0 \leq s < b$) with the relevant boundary conditions, detailed below. The contact-free segment of the rod is governed by the six rod equations, Eqs. (13) to (17), in the absence of external forces.

Similarly to the small-loading static regime, the boundary conditions at $s = 0$ are given by:

$$n_x(0) = 0 \qquad n_y(0) = f_0, \qquad m(0) = 0. \tag{22}$$

At $s = b$, boundary conditions are imposed by geometry at the touch-down location:

$$x(b) = -\frac{1+d}{2} \sin\left(\frac{\Delta\alpha}{2}\right), \qquad y(b) = \frac{1+d}{2} \cos\left(\frac{\Delta\alpha}{2}\right), \tag{23}$$

$$\theta(b) = \frac{\Delta\alpha}{2}, \qquad m(b) = -\xi \frac{2}{1+d}. \tag{24}$$

The two latter boundary conditions correspond, respectively, to the continuity of the rod tangent and its curvature. Finally, the two unknown parameters of our system of equations, b and $\Delta\alpha$, are linked from geometry as:

$$b = \frac{\ell}{2} - \frac{\Delta\alpha(1+d)}{4}. \tag{25}$$

The system of six equations governing the contact-free region, Eqs. (13)–(17), with the two unknown parameters, b and $\Delta\alpha$, was solved using the seven boundary conditions described in the relations of Eq. (22) to (24), along with the compatibility equation of Eq. (25).

We now focus on the mechanics of the contact region ($b \leq s \leq \ell/2$). We seek to express the distributed contact force $\mathbf{p}(s)$ applied by the cylinder onto the rod, and the internal tension of the rod, $n_1(s)$. Since contact is frictionless, the contact force is purely normal to the cylinder surface and therefore has no tangential component, *i.e.*, $p_1 = 0$, and no external torque is applied either ($\mathbf{q} = \mathbf{0}$). Moreover, the curvature of the rod centerline is constant and geometrically bounded to be $\kappa(s) = -2/(1+d)$. Substituting $\kappa' = 0$ and $\mathbf{n} = n_1 \mathbf{d_1} + n_2 \mathbf{d_2}$ into Eq. (16), we find that the shear force of the rod in the contact region is $n_2 = 0$. Since shear force at the end of the contact-free segment, $n_2(b^-)$, is finite, a concentrated force λ_b must be applied by the cylinder onto the rod to ensure the jump in shear force, such that:

$$\lambda_{b2} = n_2(b^-), \tag{26}$$

according to the jump condition Eq. (18) with $n_2(b^+) = 0$. Since contact is frictionless, we have $\lambda_{b1} = 0$.

Next, the rod equation describing balance of force, Eq. (15), projected along $\mathbf{d_1}$, predicts the vanishing rate of change of the tension, $n_1' = 0$. In the contact region, the tension is therefore constant and equal to the tension at the touch-down location,

$$n_1(s) = n_1(b). \tag{27}$$

Finally, by projecting Eq. (15) onto $\mathbf{d_2}$, we relate the distributed contact force applied by the rigid cylinder with the curvature of the contact region:
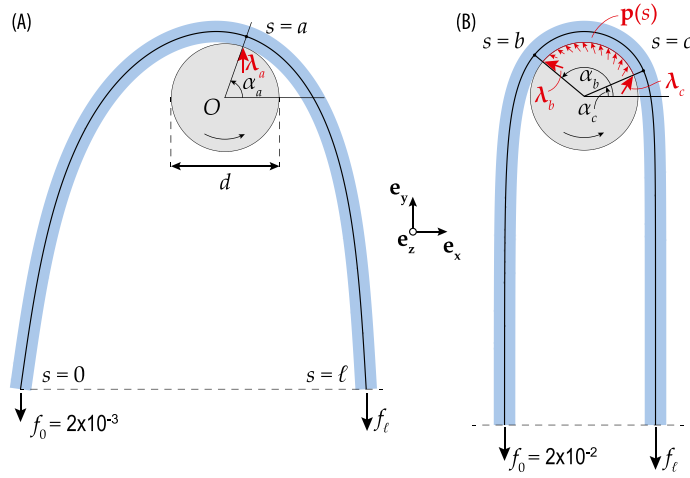
$$p_2(s) = -\kappa n_1 = \frac{2 n_1}{1+d}. \tag{28}$$

Fig. 8. Schematic representation of the sliding case, with friction. **(A)** Small-loading sliding regime. At $f_0 = 2\times10^{-3}$, the elastic rod only comes into contact with the cylinder at a single arclength $s = a$. At this contact location, the cylinder applies a frictional concentrated force, λ_a, to the rod. **(B)** Large-loading sliding regime. At the $f_0 = 2\times10^{-2}$, the contact geometry is characterized by an extended line, ranging from arclength $s = b$ to $s = c$. The cylinder applies the concentrated forces λ_b and λ_c at $s = b$ and $s = c$, as well as a distributed (frictional) contact force $\mathbf{p}(s)$ between b and c. In the text, we show that $\lambda_b = 0$.

Note that the relations describing the rod in the contact region, Eqs. (26)–(28), require no additional numerical integration as they are dictated by the results of the contact-free segment.

To summarize the theoretical procedure of the static case, solving the ODEs enabled the theoretical prediction of the transition force from a single point to extended contact region, $f_0^\star$, as well as the extent of the contact region, $\Delta\alpha$. These two quantities will be compared with experiments and numerics in Section 5.

4.3. Sliding frictional case

We now model the rod in the sliding case. To emulate the frictional interaction, we assume that the rigid cylinder rotates anti-clockwise around its axis. Simultaneously, the rod is kept in place by the loading force, f_0, at $s = 0$, while the height of the other extremity is fixed at $y(\ell) = y(0)$ by the unknown vertical force f_ℓ (reminiscent of the driving force in the experimental and numerical frameworks). To further mimic the physical and numerical experiments, the frictional interaction between the rod and the cylinder will be included through an Amontons–Coulomb friction law (with a kinematic friction coefficient, $\mu = 0.35$). Finally, we will again consider that the contact geometry transitions from a single point at small values of f_0 to an extended contact line for larger values of f_0. We will characterize the transition loading force, $f_0^\star$, separating the corresponding small and large loading regimes.

In Fig. 8, we provide a schematic representation of both the single-contact point configuration (Fig. 8A at $f_0 = 2\times10^{-3}$) and the extended-contact line configuration (Fig. 8B at $f_0 = 2\times10^{-2}$). The shape of the rod is now asymmetric with respect to the y-axis, due to the frictional interaction. Hence, unlike the model of the static case presented in the previous section, we must consider the entire rod ($0 \leq s \leq \ell$). First, in Section 4.3.1, we derive the set of ODEs for the case of a single contact point (small-loading regime). Then, in Section 4.3.2, we focus on the case of an extended contact line (large-loading regime), where we show that a distributed contact force in the contact region must be complemented by potential concentrated forces at the touch-down and lift-off locations (at $s = b$ and $s = c$, respectively).

4.3.1. Small-loading sliding regime: a single contact point

For small values of the loading force, f_0, the rod enters in contact with the rigid cylinder at a single point, at the unknown arclength $s = a$ (located at an angle α_a with respect to the horizontal axis). The cylinder applies a frictional concentrated force $\lambda_a = \lambda_{a1}\mathbf{d_1} + \lambda_{a2}\mathbf{d_2}$ (with the Amontons–Coulomb relation $\lambda_{a1} = -\mu\lambda_{a2}$). Away from the contact point, there are not external force and, therefore, the two regions $0 \leq s < a$ and $a < s \leq \ell$ are governed by the classic elastica equations, Eqs. (13)–(17), in the absence of external forces and moments. To solve these six equations in the two contact-free segments, along with the three unknown parameters of the system, s_a, α_a and λ_{a2}, we need to express the necessary nine boundary and matching conditions, as detailed next.

First, the boundary conditions at $s = 0$ and $s = \ell$ are

$$n_x(0) = 0, \qquad n_y(0) = f_0, \qquad m(0) = 0, \tag{29}$$

and

$$y(\ell) = y(0), \qquad n_x(\ell) = 0, \qquad m(\ell) = 0. \tag{30}$$

Note that we imposed $y(\ell) = y(0)$ to reproduce the numerical setup, where the vertical displacements of the two extremities were set to be equal. Next, the geometrical matching conditions of continuity at $s = a$ are expressed as a function of the known cylinder diameter d and the unknown angle α_a:

$$x(a^-) = \frac{1+d}{2} \cos \alpha_a, \qquad y(a^-) = \frac{1+d}{2} \sin \alpha_a, \qquad \theta(a^-) = \alpha_a - \frac{\pi}{2}, \tag{31}$$

where $x(s), y(s)$, and $\theta(s)$ are continuous at $s = a$;

$$x(a^+) = x(a^-), \qquad y(a^+) = y(a^-), \qquad \theta(a^+) = \theta(a^-). \tag{32}$$

Finally, recalling Eqs. (18) and (19), the force and moment jump conditions imposed by the concentrated force λ_a are

$$n_1(a^+) = n_1(a^-) + \mu \lambda_{a2}, \qquad n_2(a^+) = n_2(a^-) - \lambda_{a2}, \qquad m(a^+) = m(a^-) + \frac{1}{2}\mu \lambda_{a2}. \tag{33}$$

We solved the system of six ODEs of the two contact-free segments ($0 \leq s < a$ and $a < s \leq \ell$), while also solving for the three unknown parameters s_a, α_a and λ_{a2}. Similarly to the static case, we monitored the curvature profile along the rod arclength during the computations, as the loading force, f_0, was increased. The maximum (absolute) value of curvature always occurred at $s = a^-$, and the single contact-point model ceased to be valid when the curvature $\kappa(a^-)$ reached the critical value $\kappa^\star = -2/(1+d)$ (corresponding to the curvature of a rod fully wrapped around the cylinder). Beyond this critical transition force, when $f_0 = f_0^\star$, we used the large-loading sliding regime to model the contact model region, presented next.

4.3.2. Large-loading sliding regime: an extended contact line

When $f_0 > f_0^\star$, the contact line spans over $b \leq s \leq c$. To model this configuration efficiently, we split the rod into three segments. The mechanics of the two contact-free segments ($0 \leq s \leq b$ and $c \leq s \leq \ell$) are governed by the elastica Eqs. (13) to (17) in the absence of external forces and moments. In the contact region ($b \leq s \leq c$), a distributed contact force, $\mathbf{p}(s)$, is applied at the rod surface (as presented schematically in Fig. 8B). Similarly to the previous static case (Section 4.2) and as proposed by Stuart (1961), concentrated forces may arise at the locations of touch-down and lift-off (at $s = b$ to $s = c$, respectively). We now derive the set of ODEs governing the shape of the rod and the force transmission within the contact region. First, we will focus on the effect of the distributed contact force, $\mathbf{p}(s)$. Then, we will discuss the presence of concentrated forces at the touch-down and lift-off locations. Finally, we will express the boundary and matching conditions necessary to solve the system of ODEs with the identified unknown parameters of the system.

Governing Equations inside the Contact Region

Within the contact region ($b \leq s \leq c$), the kinematics of the rod are dictated by the two relations between centerline position and the rotation angle, Eqs. (13) and (14), in addition to the geometrical constraint on the curvature

$$\theta'(s) = -\frac{2}{1+d}. \tag{34}$$

The forces and moments balance equations, Eqs. (15) and (16), respectively, need to be adjusted to account for the presence of the frictional contact force, $\mathbf{p}(s) = p_1(s)\mathbf{d_1}(s) + p_2(s)\mathbf{d_2}(s)$, with the Amontons–Coulomb friction law: $p_1 = -\mu p_2$. Moreover, $\mathbf{p}(s)$ induces the distributed external torque on the centerline,

$$\mathbf{q} = -\frac{1}{2}\mu p_2 \mathbf{d_3}. \tag{35}$$

Given that the curvature in the contact region, κ, is constant, the next step is to substitute $\kappa' = 0$, $\mathbf{q}$, and $\mathbf{n} = n_1\mathbf{d_1} + n_2\mathbf{d_2}$ into the moment balance equation, Eq. (16). Upon projecting this relation onto $\mathbf{d_3}$, we obtain the relation between the internal shear force (n_2) and the normal reaction force (p_2) applied by the rigid cylinder to the rod:

$$n_2 - \frac{1}{2}\mu p_2 = 0. \tag{36}$$

Using this result, we now decompose the force balance relation, Eq. (15), along the director vectors $\mathbf{d_1}$ and $\mathbf{d_2}$ as

$$n_1'(s) = 2n_2(s)\frac{d}{1+d}, \tag{37}$$

$$n_2'(s) = n_1(s)\frac{2}{1+d} - n_2(s)\frac{2}{\mu}. \tag{38}$$

These two ODEs govern the evolution of the rod internal force in the contact region and are equivalent to the single second-order ODE (21) derived by Jung et al. (2004, 2008a). In these two studies, the authors focused mainly on the distributed force along the contact region but did not account for the effect of potential concentrated forces arising at the locations of touch-down and lift-off, as suggested earlier by Stuart (1961). These concentrated forces must be taken into account to develop a quantitative description of the system and enable a direct comparison with physical and numerical experiments, as detailed next.

Concentrated Contact Forces at the Touch-Down and Lift-Off Locations: We now account for the concentrated forces at touch-down and lift-off ($s = b$ and $s = c$, respectively) to write the appropriate matching conditions between the contact and contact-free segments of the rod. We will first make use of a geometrical argument to show that the concentrated force at the touch-down location, λ_b, must vanish. At the lift-off location ($s = c$), the concentrated force λ_c will remain as an unknown parameter of the system.

The frictional concentrated force λ_b induces a concentrated torque at $s = b$, which, in turn, generates the jump of internal moment

$$m(b^+) - m(b^-) = \frac{1}{2}\mu\lambda_{b2}. \tag{39}$$

Employing the curvature–moment relation, Eq. (17), and making use of Eq. (34), we find $m(b^+) = -2\xi/(1 + d)$. As a reminder, the quantity ξ corresponds to the dimensionless bending stiffness of the rod. Eq. (39) then yields the curvature immediately prior to touch-down:

$$\theta'(b^-) = -\frac{2}{1 + d} - \frac{\mu\lambda_{b2}}{2\xi}. \tag{40}$$

However, the condition of non-penetration of the rod into the cylinder outside the contact region imposes $\theta'(b^-) \geq -2/(1 + d)$, or $\lambda_{b2} \leq 0$. Finally, since λ_{b2} cannot take a negative value (there is no adhesion between rod and cylinder), it follows that $\lambda_{b2} = 0$, i.e. $\lambda_b = \mathbf{0}$.

At the other end of the contact region (lift-off location, $s = c$), the geometric argument of non-penetration is not applicable. Indeed, following the same derivation at $s = c$, we obtain

$$\theta'(c^+) = -\frac{2}{1 + d} + \frac{\mu\lambda_{c2}}{2\xi}. \tag{41}$$

Therefore, the concentrated torque generated by λ_c induces a decrease of the absolute value of curvature right after the contact region (at $s = c^+$); the rod is lifted "away" from the cylinder. When writing the matching conditions between the contacting and the contact-free regions of the rod, λ_c will appear as an unknown parameter of the system.

Boundary and Matching Conditions: The boundary conditions at $s = 0$ and $s = \ell$ were provided in the previous section by the six relations of Eqs. (29) and (30). Next, we list the matching conditions of the rod at points $s = b$ and c:

(i) The position and rotation angle of the centerline at $s = b^-$ are:

$$x(b^-) = \frac{1 + d}{2}\cos\alpha_b, \qquad y(b^-) = \frac{1 + d}{2}\sin\alpha_b, \qquad \theta(b^-) = \alpha_b - \frac{\pi}{2}. \tag{42}$$

(ii) We have shown above that the concentrated force λ_b must vanish, thus ensuring the continuity of the internal moment at the touch-down location. Inside the contact region, the moment is bounded by $m(b^+) = -2\xi/(1 + d)$, and, therefore,

$$m(b^-) = -\frac{2\xi}{(1 + d)}. \tag{43}$$

(iii) The centerline position, rotation angle, and internal forces are continuous at $s = b$:

$$x(b^+) = x(b^-), \qquad y(b^+) = y(b^-), \qquad \theta(b^+) = \theta(b^-). \tag{44}$$

$$n_1(b^+) = n_1(b^-), \qquad n_2(b^+) = n_2(b^-). \tag{45}$$

(iv) The final rotation angle of the centerline in the contact region (at $s = c$) is related to the unknown parameters α_c through

$$\theta(c^-) = \alpha_c - \frac{\pi}{2}. \tag{46}$$

(v) The position and rotation angle of the centerline at $s = c^+$ are:

$$x(c^+) = \frac{1 + d}{2}\cos\alpha_c, \qquad y(c^+) = \frac{1 + d}{2}\sin\alpha_c, \qquad \theta(c^+) = \alpha_c - \frac{\pi}{2}. \tag{47}$$

(vi) Finally, the concentrated force, λ_c, induces jumps in the internal force and moment:

$$n_1(c^+) = n_1(c^-) + \mu\lambda_{c2}, \qquad n_2(c^+) = n_2(c^-) - \lambda_{c2}, \qquad m(c^+) = -\frac{2\xi}{(1 + d)} + \frac{\mu\lambda_{c2}}{2}. \tag{48}$$

The set of six boundary conditions listed above and sixteen matching conditions are necessary to solve the six ODEs of both contact-free segments, Eqs. (13)–(17) with $\mathbf{p} = \mathbf{q} = \mathbf{0}$, and, the five ODEs of the contact region Eqs. (13), (14), (34), (37), and (38). Note that this system is augmented by the five unknown parameters, b, c, α_b, α_c, λ_{c2}. We solved the system of ODEs with unknown parameters for increasing values of the loading force, $1\times10^{-4} < f_0 \leq 0.1$.

In Section 6, we will present results supporting that for large enough cylinder diameters ($d \gtrsim 5$), the model developed in this section yields a excellent predictions for the force ratio, f_ℓ/f_0, for a wide range of loading forces, f_0.

5. Results for the static case

Having described our experimental (Section 3.1), computational (Section 3.2), and theoretical (Section 4) tools, we proceed by comparing the results of these three approaches for the static case, when no frictional sliding occurs between the rod and the cylinder. First, in Section 5.1, we will show that both the FEM-computed distributed force profile at the cylinder surface and the internal force of the rod are reproduced accurately by the elastica. Then, in Section 5.2, we will focus on the total and reduced wrapping angles, comparing the experimental and the FEM results to the wrapping angle predicted by theory.
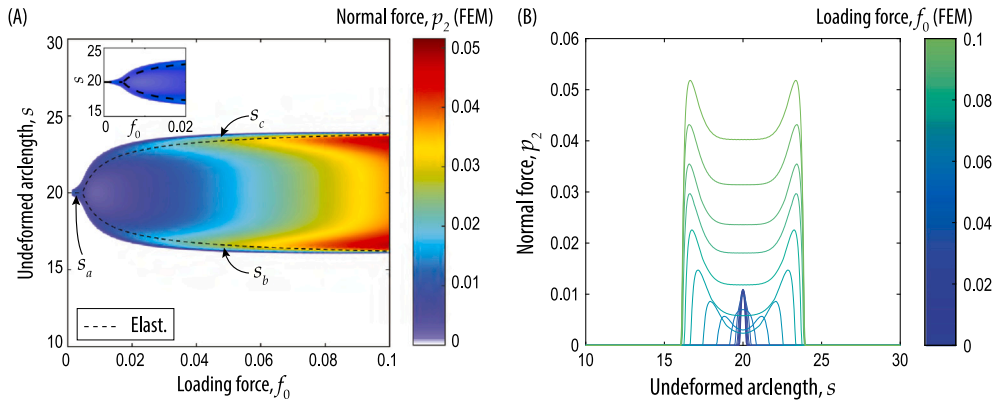
Fig. 9. Distributed normal contact force, p_2, along the arclength, s, for varying loading forces, f_0, in the static case, for $d = 5$. (A) Surface plot of the normal contact force p_2. The elastica predictions of the contact point, s_a, and the locations of the concentrated forces, s_b and s_c are represented as dashed lines. A zoom of the surface plot for small values of f_0 is presented in the inset. (B) Profiles of the contact force at fixed values of f_0. Note that p_2 transforms from a single force peak to a double-peaked force profile, as the loading force is increased.
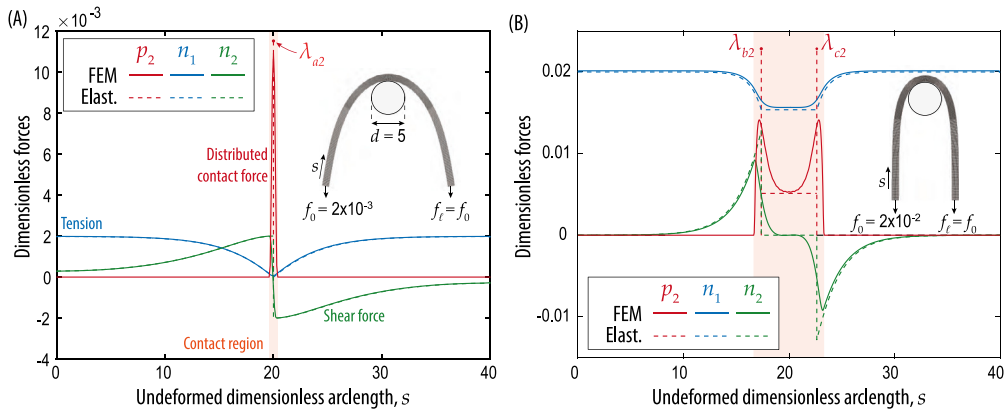

Fig. 10. Profiles of the external distributed force, $p_2(s)$, internal tension, $n_1(s)$, and internal shear force, $n_2(s)$, along the rod arclength, computed through FEM and theory at two different loading forces, f_0. (A) At $f_0 = 2 \times 10^{-3}$, the distributed force $p_2(s)$ computed from FEM is localized around $s = \ell/2 = 20$. The elastica theory predicts a single contact point at this location (small-loading regime). (B) At $f_0 = 2 \times 10^{-2}$, two smooth peaks of $p_2(s)$ are computed from the numerics and theory predicts two concentrated forces. In (A) and (B), a snapshot of the front view of the FEM is provided in the inset.

5.1. Force profiles along the rod: FEM and theory

In Fig. 9, we present the FEM-computed contact force profiles, $p_2(s)$, along the rod arclength, at varying values of the loading force, f_0. In Fig. 9A, the surface plot $p_2(s)$ in the $f_0 - s$ plane shows the transition from a single contact point to an extended contact line. In addition, we represent the theoretical prediction for the location of the contact point, s_a, computed from the small-loading static regime, and the locations of concentrated forces, s_b and s_c, corresponding to the large-loading static regime. In Fig. 9B, we present sections of the surface plot of Fig. 9A, at different values of f_0. Again, we highlight the transition from single to extended contact, and we observe the emergence of two force peaks in the extended-contact regime. Next, we investigate the two contact regimes more in details.

In Fig. 10, we present the numerical (solid lines) and theoretical (dashed lines) profiles of $p_2(s)$ (red), $n_1(s)$ (blue), and $n_2(s)$ (green) for $d = 5$ at the two dimensionless loading forces, $f_0 = 2 \times 10^{-3}$ (Fig. 10A), and $f_0 = 2 \times 10^{-2}$ (Fig. 10B). There is an overall good agreement between FEM and theoretical predictions. At both loading forces, the contact force is zero outside the contact region. On the other hand, the tension and shear forces are approximately constant far away from the contact region, and undergo strong changes close to the contact region. Interestingly, the force profiles exhibit qualitative differences between the two values of f_0, which we discuss next.

At the small loading force $f_0 = 2 \times 10^{-3}$, we find that the contact force $p_2(s)$ computed from FEM (solid line) is single-peaked and localized in the contact region (around $s = \ell/2 = 20$). The elastica (dashed line) predicts this peak by the concentrated force, λ_a, of the small-loading regime ($f_0 < f_0^\star$, c.f. Section 4.2). At the larger loading force, $f_0 = 2 \times 10^{-2}$, the distributed contact force computed from FEM, $p_2(s)$, exhibits two well-defined peaks connected by a region of lower force intensity. Near these simulated force peaks, the theory (dashed line) predicts two concentrated forces, λ_b and λ_c, in the large-loading regime ($f_0 > f_0^\star$, c.f. Section 4.2). Within

the contact region (between the two concentrated forces), the distributed contact force predicted by the theoretical model is constant and close to the value of the local minimum measured from FEM.

Note that the FEM yields smoothly varying force profiles at both values of the loading forces, whereas the theoretical predictions are sharp. For example, in Fig. 10B, the shear force profile, $n_2(s)$, computed from FEM, undergoes large changes but does not exhibit sharp discontinuities. By contrast, the theory predicts that the shear force transitions from a finite value $n_2(b^-) = 0.013$ just before contact to $n_2(b^+) = 0$ past the onset of contact. The theoretical model provides a good approximation of the evolution of the force profiles (p_2, n_1 and n_2) but is unable to capture the smooth changes, which we anticipate to be due to elastic deformations of the cross-section of the physical rod under the transverse load of p_2. This cross-sectional deformation will be discussed in more detail below, in Section 5.3.

5.2. Total and reduced wrapping angles

In Fig. 11A and B, we present photographs of the experimental realizations and snapshots of the FEM of the static case for the smallest and largest dimensionless cylinder diameters that we considered ($d = 1$ and 10), under the loading force $F_0 = F_L = 1.37$ N ($f_0 = f_\ell = 0.45$). From the FEM-computed contact force distribution, p_2 (solid orange line), we extracted the total and reduced wrapping angles, $\Delta\alpha_{\text{tot}}$ and $\Delta\alpha_{\text{red}}$, respectively. As a reminder, $\Delta\alpha_{\text{tot}}$ was defined as the total extent of the contact region (where $p_2 > 0$), and $\Delta\alpha_{\text{red}}$ corresponds to the angle between the two maxima of the distributed contact force (see Section 3.2). In Figs. 11C-F, we plot the results from experiments (data points) and FEM (thick solid lines with shaded area) for the total wrapping angle, along with the reduced wrapping angle (thin solid line) computed from FEM, and the wrapping angles predicted by the elastica (dashed line) as a function of f_0 for the four dimensionless cylinder diameters $d = 1$, 2, 5, and 10. Next, we detail the results of the total and reduced wrapping angles.

We used the total wrapping angle $\Delta\alpha_{\text{tot}}$ to validate the FEM simulations against experiments. The shaded regions associated to the FEM predictions of Fig. 11 correspond to the experimental uncertainty arising from the imaging artifact due to parallax, which we described in Section 3.1.3. We recall that this artifact induced a slight overestimation of the total wrapping angle in the experiments. Taking this correction into account, we observe excellent agreement between the experiments and FEM, for the four tested dimensionless cylinder diameters, thus quantitatively validating our FEM computations in the static case.

The theory is unable to predict the *total* wrapping angles accurately. Instead, the predictions of $\Delta\alpha$ capture the *reduced* wrapping angle, $\Delta\alpha_{\text{red}}$, of the physical rod significantly more accurately, especially for the larger cylinder diameters, $d = 5$ and $d = 10$. Theory predicts two concentrated forces, λ_b and λ_c, at the touch-down and lift-off locations. For the physical rod, these concentrated forces are smoothed out into distributed force peaks due to the deformation of the cross-section and contact extends further than the force peaks. Therefore, theory provides a good approximation for the location of these peaks (which define $\Delta\alpha_{\text{red}}$) but is unable to accurately predict $\Delta\alpha_{\text{tot}}$. Also, the theoretical transition forces $f_0^\star$ between the small and large-loading regimes correspond closely to their numerical counterpart (see closed vs. open star-points in the plots), suggesting that the theory provides a good approximation of the backbone of the physical problem. Note that for the smaller cylinder diameters $d = 1$ and $d = 2$, the wrapping angles calculated from theory display a discrepancy with the $\Delta\alpha_{\text{red}}$. This mismatch stems from the higher curvatures of the deformed rod, $\kappa \sim 1$, which are not accounted for in the theoretical models.

5.3. Cross-section deformation of the physical rod

The physical elastic rod can undergo cross-sectional deformations under high curvatures and external forces applied by the cylinder. Such deformations, which can be investigated through FEM, are not accounted for by the Euler's elastica considered in the present study. This difference is likely at the source of the discrepancies between theory and FEM. The importance of cross-sectional deformations when modeling the onset of contact between a rod and a rigid substrate was previously investigated by Naghdi and Rubin (1989). In their study, the authors focused on linearized beam equations and showed that a centerline-based model that neglects transverse deformations could not predict the continuous contact force profile at touch-down or lift-off, as it leads to discontinuities similar to the ones predicted by our elastica model. In the future, building up on the work by Naghdi and Rubin (1989), more extended modeling efforts to include transverse deformations into Euler's elastica would likely yield a more accurate representation of the rod-cylinder contact mechanics near touch-down and lift-off.

To provide further insights toward future improvements in the modeling of elastic rods, we take advantage of our FEM results to report the shape changes of the rod middle cross-section under loading. In Fig. 12A, we provide a snapshot of FEM for the extreme diameter $d = 1$, at the loading force $f_0 = 0.02$, and highlight the location of the cutting plane to generate cross-sectional views of the rod at $s = \ell/2$. The resulting middle cross-sections are presented in panels B1 to E3 for the four values of diameters considered ($d = 1$, 2, 5, and 10) at the loading forces $f_0 = 0.02$, 0.05, and 0.10. For comparison, we also represent the initial square cross-section of the rod in its rest configuration (colored squares).

For $d = 1$, the cross-section undergoes large deformations, even at the relatively small loading force $f_0 = 0.02$ (Fig. 12B1). Due to the large curvature involved, the section displays an *anticlastic* curvature, characterized by an upward lift-up of the section near its free sides, as commonly observed in bent elastic plates (Audoly and Pomeau, 2010). When the loading force is increased (Fig. 12B2 at $f_0 = 0.05$ and Fig. 12B3 at $f_0 = 0.10$), this deformation becomes even more pronounced. For larger cylinders, the cross-sectional deformations become less important. For example, for $d = 10$ and $f_0 = 0.02$ (Fig. 12E1), the deformed cross-section is almost indistinguishable from its rest shape. We note that, in addition to the slight anticlastic curvature observed in each sectional view, the area of the cross-section always appears smaller than the rest configuration. This decrease in area is explained by the extensional
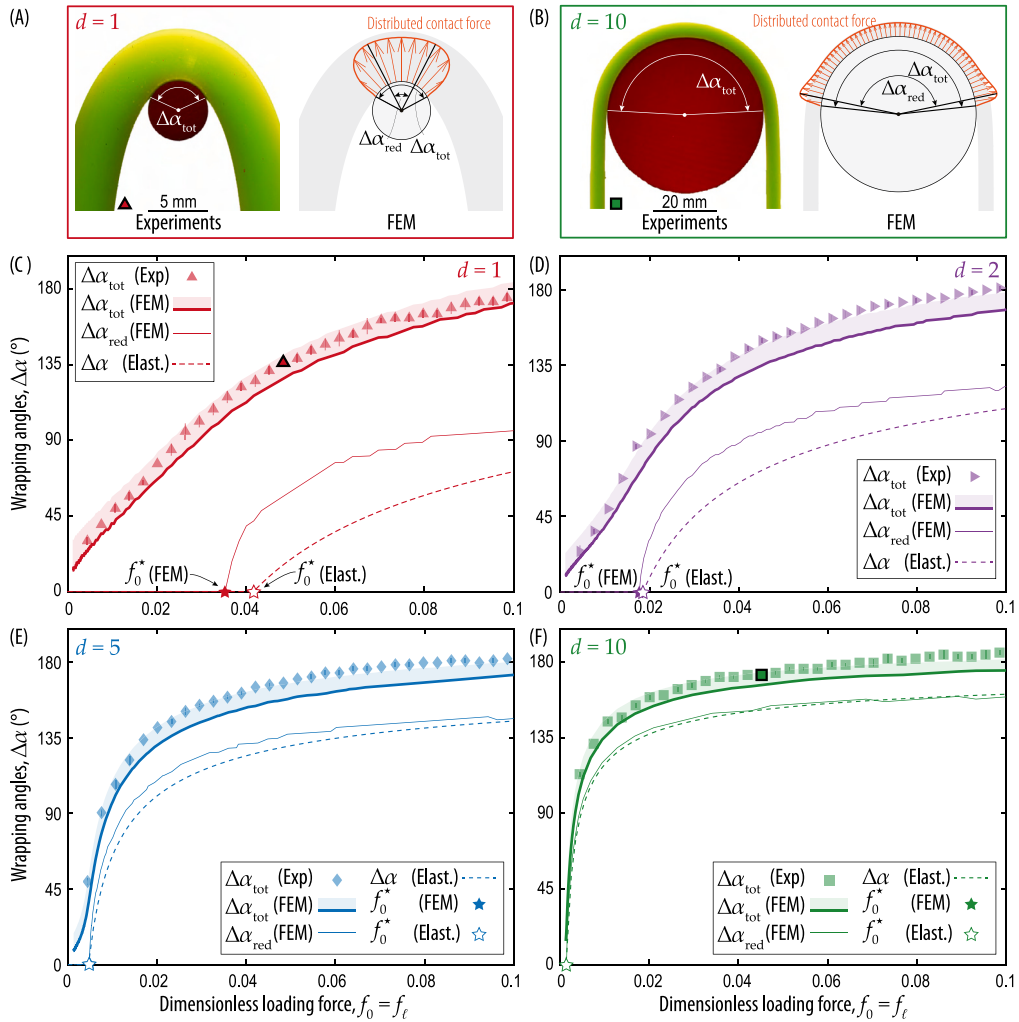
Fig. 11. Total and reduced wrapping angles in the static case. (A) Photograph of the experimental realization and snapshot of the FEM computation for a cylinder diameter $D = 5$ mm ($d = 1$) at a loading force $F_0 = F_L = 1.37$ N ($f_0 = f_\ell = 0.045$). The total wrapping angle, $\Delta\alpha_{tot}$, is represented in the experimental and numerical configurations. The reduced wrapping angle, $\Delta\alpha_{red}$, is computed from the maxima of the distributed contact force represented as an orange solid line in polar coordinates around the surface of the cylinder in the FEM snapshot (in arbitrary units). (B) Same information as in panel (A) with $D = 50$ mm ($d = 10$). (C) to (F) Total and reduced wrapping angles as a function of the dimensionless loading force f_0. The data points and the thick solid lines with shaded areas correspond to the total wrapping angle measured experimentally and computed numerically, respectively. The shaded areas represent the uncertainty attributed to experimental measurements. The reduced wrapping angle extracted from FEM is represented by the thin solid lines. The dashed lines correspond to the theoretical predictions based on Euler's elastica. The transition force, $f_0^\star$, at which the contact region starts growing from a localized point to an extended line, is highlighted for each diameter as a filled star for FEM and a hollow star for the elastica. The data corresponding to the photographs and snapshots of panels (A) and (B) are highlighted in the plots of (C) and (F).

stretching of the rod under tension, which leads to shrinking in the transverse directions under the constraint of volume conservation due to the incompressibility of the elastomer (Poisson's ratio, $\nu = 0.5$). Both the emergence of anticlastic curvature and the reduction of the cross-section area likely affect the overall load transmission along the deformed rod.

Building on the observed shape changes, the elastica model could be improved in future works, e.g., by taking local deformations into account under the effect of tension (stretching), curvature (anticlastic curvature), or transverse loading through contact forces. However, these developments go beyond the scope of the present study.

6. Results for the sliding case

We now turn to the sliding case, when the rod is set to slide continuously at the surface of the rigid cylinder. Under this frictional interaction, differently from the static case, the system is no longer symmetric around the y-axis. Furthermore, the loading force, f_0, and driving force, f_ℓ, applied at the ends $s = 0$ and $s = \ell$, respectively, are not equal. We will report how the f_ℓ/f_0 ratio depends on the cylinder diameter and on the loading force, f_0. First, in Section 6.1, we will start by comparing the FEM and
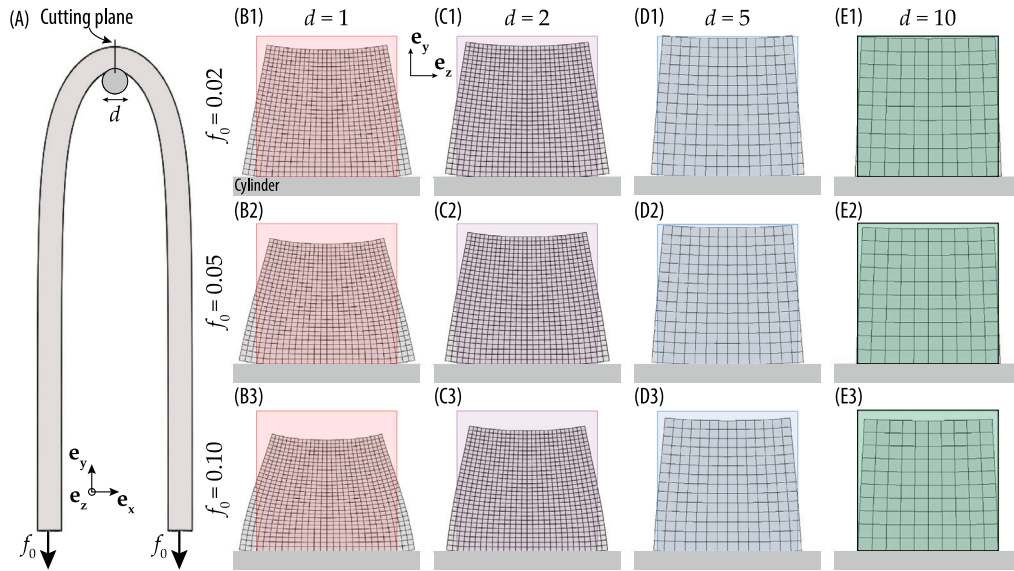
Fig. 12. Middle cross-section deformation of the mid-section for different dimensionless cylinder diameters, d, and under varying loading forces f_0. (A) Front view of FEM for $d = 1$ and $f_0 = 0.02$. In panels (B1) to (E3), we present the cross-sectional views of the rod mid-section (the cutting plane is highlighted in A) for dimensionless cylinders $d = 1$, 2, 5, 10 (letters B to E, respectively), under the loading forces $f_0 = 0.02$, 0.05, and 0.10 (numbers 1 to 3, respectively). The rest cross-section shape of the rod is represented by the superposed shaded colored squares.

theoretical predictions of the evolution of the external and internal forces along the rod. Then, in Section 6.2, we will perform a direct comparison of f_ℓ / f_0, as a function of f_0, between the experiments, FEM, and theory for a set of different cylinder diameters.

6.1. Profiles of the external and internal forces: FEM and theory

In the frictional sliding case, the distributed external force applied by the cylinder onto the rod, $\mathbf{p}(s)$, is characterized by a tangential, $p_1(s)$, and a normal, $p_2(s)$, component which are related by the Amontons–Coulomb friction law, $p_1(s) = -\mu p_2(s)$ through the kinematic friction coefficient, μ. For brevity, we will only report the normal component, p_2. In Fig. 13, we present the evolution of the contact force profiles computed from FEM, as the loading force, f_0, is varied. In Fig. 13A, the surface plot suggests that, similarly to the static case, the nature of the contact region transitions from a single point to an extended contact region. Again, this transition is captured by the theory, as demonstrated by the prediction (dashed lines) corresponding to the location of the single contact point, s_a, of the small-loading sliding regime, and the locations of touch-down, s_b, and lift-off, s_c, in the large-loading sliding regime. Note that for $f_0 \gtrsim 0.04$, s_b starts diverging from the FEM-computed touch-down location, which we attribute to the extensibility effect of the simulated elastomeric rod, not accounted for in the elastica theory. In Fig. 13B, the contact force profiles at different values of the loading force, f_0, further demonstrate this transition and the emergence of two force peaks as the loading force is increased. The increase of the distributed force within the contact region stems from the frictional interaction with the cylinder. Next, we compare the FEM-computed and theoretical force profiles in the small- and large-loading regimes.

In Fig. 14, we present the profiles of p_2 along with the internal tension, n_1, and shear force, n_2, of the rod. By way of example, we focus on representative values of the loading force: $f_0 = 2 \times 10^{-3}$ (Fig. 14A) and $f_0 = 2 \times 10^{-2}$ (Fig. 14B). Similarly to the frictionless static case, as the loading force is increased, we observe that the nature of the contact transitions from a localized point to an extended region. At the two values of the loading forces considered, the theoretical tension and shear force profiles capture their FEM counterparts accurately. It is important to note that the theoretical tension profiles exhibit discontinuities. For example, at $f_0 = 2 \times 10^{-2}$, the tension jumps from a value $n_1(s = c^-) = 3.4 \times 10^{-2}$ to $n_1(s = c^+) = 4 \times 10^{-2} > n_1(s = c^-)$, as highlighted in Fig. 14B. The signature of these sharp changes in tension is also observed in the FEM tension profile, albeit in a smoother manner, likely due to the deformation of the cross-section.

When $f_0 = 2 \times 10^{-3}$ (Fig. 14A), FEM predicts a small contact region, characterized by a peak of normal force $p_2(s)$ at $s = 21.80$. This peak is captured by the elastica, which predicts the concentrated force, λ_a, at $s = a = 21.87$. It is important to recall that the theory has no adjustable parameters, which makes this excellent agreement even more remarkable. Further, the FEM results show that the tension of the rod, n_1, reaches a negative value just before the contact location, after which it increases sharply under the effect of the frictional contact point. This abrupt change in tension is accurately reproduced by the theory. Note that despite the relatively small loading, the extremities of the rod are nearly aligned with the two vertical end forces, as observed in the snapshot of the FEM computation (inset of Fig. 14). Consequently, $n_1(s = 0) \simeq f_0$ and $n_1(s = \ell) \simeq f_\ell$ and n_2 is close to zero at the rod extremities.
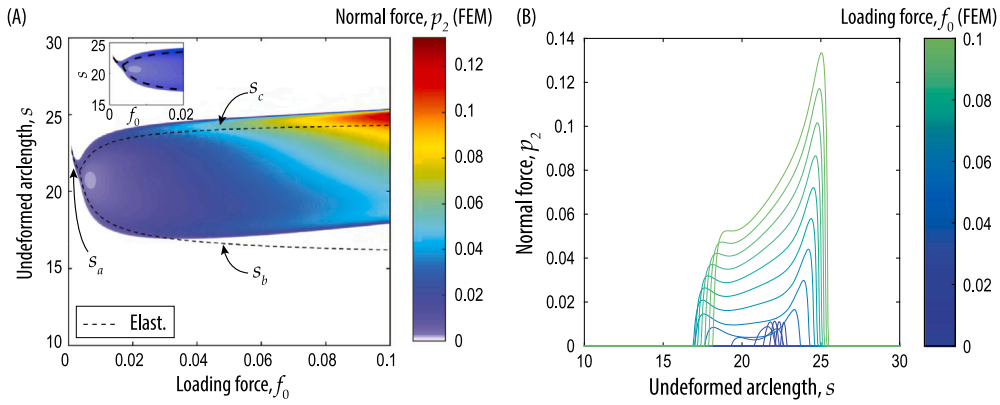
Fig. 13. Distributed normal contact force, p_2, along the arclength, s, for varying loading forces, f_0, in the sliding case. (A) Surface plot of the contact force. The elastica predictions of the contact point, s_a, and the locations of the concentrated forces, s_b and s_c are represented as dashed lines. A zoom of the surface plot for small values of f_0 is presented in the inset. (B) Profiles of the contact force at fixed values of f_0. Note the transition from a single force peak to a double-peaked force profile as the loading force is increased.
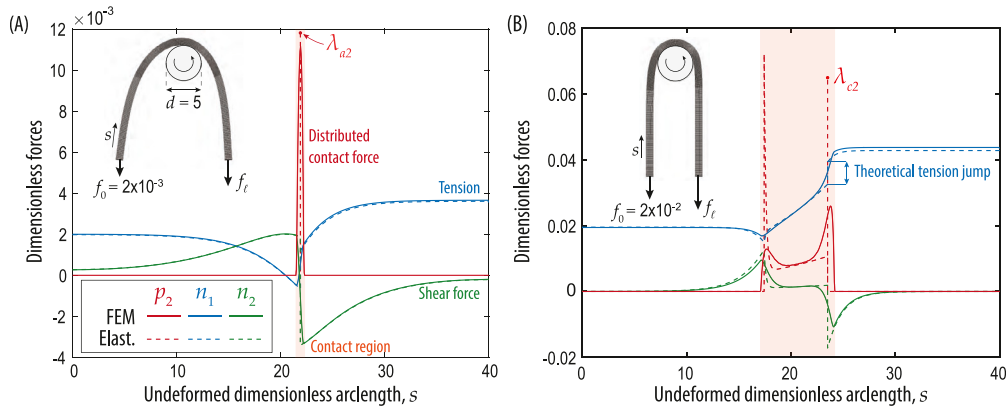

Fig. 14. Profiles of the external distributed contact force, p_2, internal tension, n_1, and internal shear force, n_2, along the rod arclength for a dimensionless cylinder diameter $d = 5$ at two different loading forces, f_0. The loading force is $f_0 = 2 \times 10^{-3}$ in (A) and $f_0 = 2 \times 10^{-2}$ in (B). The forces, p_2 (red), n_1 (blue), and n_2 (green) are represented as solid and dashed lines for FEM configuration and the elastica theory, respectively. A front view of the FEM is provided in both panels as insets.

When the loading force is increased to $f_0 = 2 \times 10^{-2}$ (Fig. 14B), the FEM results predict an extended contact region, with two peaks in the distributed contact force at $s = 17.64$ and $s = 23.80$, connected by an increasing ridge. The theory captures well the second force peak through the concentrated force λ_c (at $s = c = 23.52$). By contrast, the first FEM force peak ($s = b = 17.40$) is not associated to any theoretical concentrated force. Indeed, building on a geometrical argument, in Section 4.3, we demonstrated that $\lambda_b = 0$. Still, at the onset of contact ($s = b = 17.40$), the theoretical model predicts a high (but finite) value of the distributed contact force, which decays continuously past the onset of contact. After the decay around $s \simeq b$, the theoretical prediction of $p_2(s)$ then increases slightly throughout the contact region, closely following the evolution of the FEM-computed contact force. This continuous but non-monotonic behavior of p_2 at $s \simeq b$ (continuous decrease and increase) is consistent with the prediction of Jung et al. (2004).

Similarly to the static case (Section 5), the theory provides an accurate approximation of the profile of the external and internal forces, showing some dissimilarities near touch-down and lift-off. Again, we speculate that, under the effect of cross-section deformations, the force profiles computed from FEM correspond to a smoothed-out version of the theoretical prediction due to the cross-sectional deformation of the physical rods.

6.2. Driving-to-loading force ratio: Comparison between experiments, FEM and theory

In Fig. 15, we provide a more exhaustive comparison between the experimental, numerical and theoretical results, focusing on the driving-to-loading force ratio, f_ℓ/f_0 as a function of the loading force f_0, for dimensionless cylinder diameters of $d = 1, 2, 5$, and 10 (respectively in Fig. 15A, B, C, and D). First, we note that the experimental measurements (data points) are reproduced accurately by FEM with a kinematic friction coefficient $\mu = 0.35 \pm 0.02$ (solid lines and associated shaded regions), again pointing to the high fidelity of the numerical procedure. For the values of the cylinder diameter investigated, the ratio f_ℓ/f_0 computed
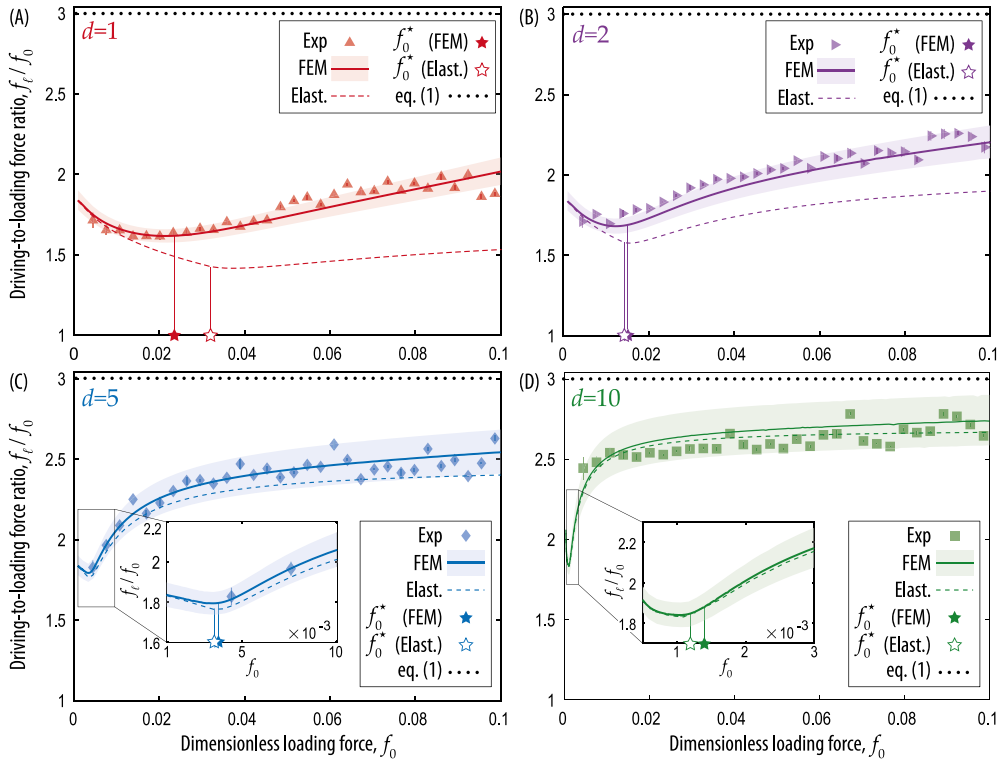
Fig. 15. Experimental measurement, numerical computation, and theoretical prediction of the driving-to-loading force ratio, f_ℓ / f_0, as a function of the dimensionless loading force, f_0, for a set of four dimensionless cylinder diameters, d. In (A), $d = 1$, in (B), $d = 2$, in (C), $d = 5$, and in (D), $d = 10$. Panels (C) and (D) provide an inset with a close-up of the plot at small loading forces. The solid lines and the associated shaded regions represent the FEM results with the corresponding confidence interval based on the mean and standard deviation of the experimental friction coefficient, $\mu = 0.35 \pm 0.02$. The data points correspond to the experimental measurements. The solutions of the elastica equations are reported as dashed lines. The horizontal dotted lines represent the constant prediction of the classic capstan equation, Eq. (1), for an ideal string with $\mu = 0.35$ and $\Delta\alpha = \pi$. The full and hollow star symbols reported on the horizontal axis, in the inset for (C) and (D), correspond, respectively, to the transition force, $f_0^\star$, computed using FEM and the elastica. At this loading force, $f_0^\star$, the contact region transitions from localized to extended.

numerically varies non-monotonically (first decreasing then increasing) with f_0, with a consistent minimum for all the cases. In the plots of Fig. 15, we also provide the prediction (horizontal dotted lines) of the ideal capstan prediction given by Eq. (1) for a perfectly thin and flexible filament, using $\mu = 0.35$ and $\Delta\alpha = \pi$. The latter is chosen to reflect the vertical orientation of the end forces. The classic capstan equation overestimates the force ratio significantly, especially for decreasing cylinder diameters.

Euler's elastica (dashed lines) captures FEM accurately for the two larger diameters $d = 5$ and 10. For $d = 1$ and 2, however, a quantitative mismatch appears between the numerical and theoretical approaches. As mentioned in Section 5, this mismatch is rooted in the assumption of the elastica model that the rod curvature remains small compared to its thickness, which is not respected for small cylinder diameters, where $\kappa \sim 1$. In addition to the large curvatures, the rod is likely to be subjected to consequent cross-section deformations (as observed in Fig. 12), further compromising the accurate modeling for small cylinder diameters.

Finally, we discuss the non-monotonic evolution of the force ratio by focusing on the geometry of the contact region. In the four plots of Fig. 15, we highlight the values of the force $f_0^\star$ at which the FEM and theoretical contact regions transition from a localized point to an extended region (full and hollow star symbols, respectively). First, we remark that the theoretical transition forces provide an accurate prediction of the FEM results. In addition, $f_0^\star$ is close to the loading force at which the f_ℓ / f_0 ratio reaches its minimum value. This coincidence between $f_0^\star$ and the force at which the slope of f_ℓ / f_0 changes highlights the non-trivial interplay between the force transmission along the rod and the geometry of the contact region. At small loading forces, the region of contact remains localized, and the force ratio decreases with f_0, whereas for larger loading forces, the region of contact starts extending, therefore leading to an increase in the force ratio due to the larger area of contact. Capturing this complex mechanical behavior was made possible by accounting for the *a priori* unknown contact geometry in our theoretical description.

7. An engineering case study: Belt-driven pulleys

In engineering applications, it is common for the power transmission between rotating shafts to be achieved through a belt brought in motion by a motor pulley. In these systems, it is undesirable for macroscopic slippage to occur, *i.e.*, sliding between
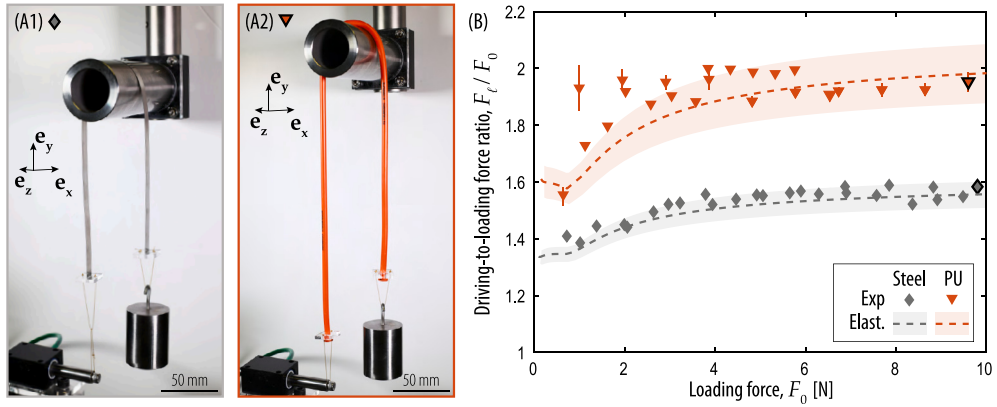
Fig. 16. Force transmission along engineering belts in contact with a rigid steel cylinder. (A) Photographs of the capstan system with the spring-steel belt (A1) and the polyurethane belt (A2), in contact with a stainless steel cylinder with $d = 250$ and $d = 8.33$, respectively. (B) Driving-to-loading force ratio, F_L/F_0, as a function of the loading force, F_0, for the two belts. The data points correspond to experiments. The dashed lines with shaded area represent the theoretical prediction based on the elastica for the experimentally measured friction coefficient and confidence interval. The values of the force ratios corresponding to the loading forces presented in the photographs of panels A1 and A2 are highlighted in the plot.

the belt and the pulleys. Indeed, slippage leads to a loss of synchronization between pulleys and can induce overheating of the belt. Predicting the maximal force ratio between the higher-tension strand and the lower-tension strand of the belt at which continuous sliding occurs is, therefore, of primary importance when designing such transmission mechanisms. In this section, we will characterize the mechanical behavior of commercially available belts in contact with a straight pulley, based on the mechanics-based framework developed earlier in the manuscript. The force ratio at which continuous sliding occurs will be investigated for a spring-steel and a polyurethane belt in contact with a stainless steel rigid cylinder. We will compare the experimentally measured values of the driving-to-loading force ratio, F_L/F_0, to the predictions of the theory. Our results suggest that the specialized elastica framework provides an accurate tool to predict the onset of slippage in belt–pulley systems.

In Fig. 16A1 and A2, we provide photographs of the experimental configuration for the spring-steel and the polyurethane belts, respectively, under loading by a mass 1 kg (corresponding to the loading force $F_0 = 9.81$ N). As we detailed in Section 3.1, the spring-steel belt has a rectangular cross-section, and the polyurethane belt is cylindrical. The kinematic friction coefficient between the pairs spring-steel/steel and polyurethane/steel were measured to be $\mu = 0.15 \pm 0.01$ and $\mu = 0.26 \pm 0.02$, respectively. The dimensionless diameter of the cylinder was $d = 250$ for the spring-steel belt and $d = 8.33$ for the polyurethane belt. Given that $d > 5$ in both cases, we expect the theory to provide an accurate description, as discussed in Section 6.

In Fig. 16B, we plot the experimental data (data points) of the force ratio, F_L/F_0, as a function of the loading force, F_0, together with the theoretical predictions from our elastica model (dashed lines). For both the spring-steel (gray points/lines in the plot) and the polyurethane (orange points/lines in the plot) belts, the theory accurately captures the increase of force ratio with the loading force; the contact region grows as the loading force is increased. For the polyurethane belt case, the higher uncertainty on the frictional coefficient led to a wider scatter of the experimental data. Still, the theory yields a satisfactory prediction of the force transmission between both rod ends. Note that the classic capstan theory ($F_L/F_0 = e^{\mu\pi}$) would predict the constant force ratios, $F_L/F_0 = 1.60$ for the spring-steel belt, and $F_L/F_0 = 2.26$ for the polyurethane belt. The derivation of a self-consistent elastica model enabled the prediction of the non-trivial relation between the force ratio and the loading force. Recalling the engineering context that motivated this case study, the maximum torque that can be transmitted between pulleys is related to the difference of forces in the high-tension and low-tension strands of the belt at the onset of sliding. Depending on the geometry of the transmission mechanism, our theoretical model can be adapted to predict the pretension that must be applied to the belt to ensure the desired torque transmission.

Thus far, we have focused on homogeneous belts of rectangular and circular cross-sections interacting with straight cylinders. It is important to note that other belt–pulley geometries, which go beyond the scope of this article, are commonly employed for power-transmission applications. For example, some high-performance belts made of a flexible rubber core are reinforced with steel fibers, providing the belt with increased axial stiffness and enabling higher pre-tensions with low extensional stretching. This enhanced pre-loading allows for an overall increase of the transmitted torque. We believe that future theoretical modeling efforts to describe such composite belts should account for the decoupled axial and bending stiffnesses. The V-belt is another geometry commonly used to improve power transmission (Belofsky, 1976). In this configuration, a circular or trapezoidal cross-section belt is wrapped around a grooved pulley, thus increasing the contact area, which in turn augments the force ratio. In the ideal case of a perfectly thin and flexible string in contact with a V-shaped pulley, it can be shown that Eq. (1) still applies, as long as the friction coefficient is corrected to be an effective friction coefficient $\tilde{\mu} = \mu/\sin(\beta/2)$, with β the angle of the V-shaped groove ($\beta = \pi$ for a straight cylinder). However, when considering the more realistic case of belts of finite thickness and bending stiffness, the effect of the V-shaped groove on the force transmission is nontrivial and deserves further investigation.

8. Discussion and conclusions

In this study, we have investigated the mechanics of contact between an elastic rod and a rigid cylinder, a scenario that is commonly referred to as the *generalized capstan problem*. Our main goal was to quantify the effect of the finite rod thickness and bending stiffness on the geometry of contact and the overall force transmission along the rod. We have focused on both the static and the sliding cases, characterized, respectively, by the absence and the presence of frictional sliding between the rod and the cylinder. In the static case, both extremities of the rod were weighted by an equal loading force, and we quantified the extent of the contact region, as well as the distributed contact force. In the sliding case, only one extremity of the rod was weighted, while a driving force was applied at the other end to induce continuous sliding. We observed a non-monotonic evolution of the driving-to-loading force ratio as a function of the loading force.

An Euler's elastica framework was adapted to provide a theoretical description of the revisited capstan problem. Contrary to the existing models developed by Stuart (1961) and Jung et al. (2004, 2008a), we took the unknown extent of the contact geometry into account, which enabled the direct comparison with experiments and numerics. Accounting for the distributed and concentrated forces applied by the cylinder onto the rod, we derived sets of ordinary differential equations (ODEs) governing the mechanics of the system in the static and sliding cases. Upon solving these ODEs numerically under the appropriate boundary and matching conditions, the theoretical results provide an accurate prediction for experiments and FEM computations for ratios of cylinder diameters to rod thickness larger than five.

In both the static and sliding cases, FEM indicated that the nature of contact transitioned from a single point to an extended contact region at the cylinder surface as the loading force was increased. This extended contact was characterized by the emergence of two peaks in the distributed contact force, appearing close to the touch-down and lift-off locations and bridged by a smaller distributed contact force. In the sliding case, the minimum value of the driving-to-loading force ratio took place at a loading force close to the transition force from single contact point to extended contact line. We demonstrated that theory was able to capture this transition behavior even for relatively small cylinder diameters. Furthermore, the details of the force profiles along the rod were also captured accurately by theory, and the peaks in the distributed contact force were captured by the concentrated forces of the theory. In the engineering context of belt-driven power transmission, we showed that our theoretical framework could be adapted to enable the rational design of belt–pulley systems to apply the correct pretension to the belt to achieve the desired torque transmission.

In the case of cylinder diameters comparable to the thickness of the rod, we found discrepancies between the behavior of the physical rod (experiments and FEM) and its theoretical counterpart. For example, the reduced wrapping angle (static case) and the driving-to-loading force ratio (sliding case) were underestimated by the theory. By analyzing the shape of a cross-section of the physical rod, we showed that the rod undergoes significant cross-section deformations under the effect of stretching, large centerline curvatures, and external contact forces. For small cylinder diameters, these nonlinear deformations go beyond the assumptions on which we built our elastica model.

We hope that our results will motivate future modeling efforts to account for the deformation of the rod cross-section. As a first step, we expect that including the shrinkage of the cross-section under the effect of (axial) stretching will further improve the accuracy of future theories. Furthermore, we believe that the present work will also serve as a basis when studying the mechanics of frictional elastic rods in more complex geometries. For example, a similar analysis could provide a predictive understanding of the contact between a belt and a pulley containing a V-shaped groove, a geometry widely used to increase the performance of power transmission. Finally, our study could also enable further understanding of knotted structures since friction between bent strands of rods plays a significant role in setting the overall performance of knots.

CRediT authorship contribution statement

Paul Grandgeorge: Conceptualization, Methodology, Experiments, Validation, Investigation, Formal analysis, Software, Writing – original draft, Writing – review & editing. **Tomohiko G. Sano:** Conceptualization, Methodology, Investigation, Writing – original draft, Writing – review & editing. **Pedro M. Reis:** Conceptualization, Methodology, Supervision, Writing – review & editing.

Declaration of competing interest

The authors declare that they have no known competing financial interests or personal relationships that could have appeared to influence the work reported in this paper.

Acknowledgments

References

Alali, A., Al-Khabbaz, A., Michael, S., Swain, M., 2018. Frictional coefficient during flossing of teeth. Dent. Mater. 34 (12), 1727–1734.

Audoly, B., Clauvelin, N., Neukirch, S., 2007. Elastic knots. Phys. Rev. Lett. 99 (16), 164301.

Audoly, B., Pomeau, Y., 2010. Elasticity and Geometry. Oxford University Press.

Ayres, P., Martin, A.G., Zwierzycki, M., 2018. Beyond the basket case: a principled approach to the modelling of kagome weave patterns for the fabrication of interlaced lattice structures using straight strips. In: Advances in Architectural Geometry 2018. Chalmers University of Technology, pp. 72–93.

Baek, C., Johanns, P., Sano, T.G., Grandgeorge, P., Reis, P.M., 2020. Finite element modeling of tight elastic knots. J. Appl. Mech. 88 (2).

Baek, C., Martin, A.G., Poincloux, S., Chen, T., Reis, P.M., 2021. Smooth triaxial weaving with naturally curved ribbons. Phys. Rev. Lett. 127 (10), 104301.

Baek, C., Reis, P.M., 2019. Rigidity of hemispherical elastic gridshells under point load indentation. J. Mech. Phys. Solids 124, 411–426.

Baek, C., Sageman-Furnas, A.O., Jawed, M.K., Reis, P.M., 2018. Form finding in elastic gridshells. Proc. Natl. Acad. Sci. USA 115 (1), 75–80.

Baser, O., Konukseven, E.I., 2010. Theoretical and experimental determination of capstan drive slip error. Mech. Mach. Theory 45 (6), 815–827.

Belofsky, H., 1976. On the theory of power transmission by V-belts. Wear 39 (2), 263–275.

Bigoni, D., 2015. Extremely Deformable Structures (CISM Lecture Notes No. 562). Springer-Verlag.

Breazeale, F., 1947. Apparatus for determining the coefficient of friction of running yarn. Text. Res. J. 17 (1), 27–31.

Bueno, M.-A., Camillieri, B., 2019. Structure and mechanics of knitted fabrics. In: Structure and Mechanics of Textile Fibre Assemblies. Elsevier, pp. 61–107.

Childs, P.R., 2019. Belt and chain drives. In: Mechanical Design Engineering Handbook. Elsevier, pp. 533–597.

Daily-Diamond, C.A., Gregg, C.E., O'Reilly, O.M., 2017. The roles of impact and inertia in the failure of a shoelace knot. Proc. R. Soc. Lond. Ser. A Math. Phys. Eng. Sci. 473 (2200), 20160770.

Dill, E.H., 1992. Kirchhoff's theory of rods. Arch. Hist. Exact Sci. 44 (1), 1–23.

Euler, L., 1769. Remarques sur l'effet du frottement dans l'equilibre. Mem. Acad. Sci. Berlin - (-), 265–278.

Eytelwein, J.A., 1832. Handbuch Der Statik Fester Körper: Mit Vorzüglicher Rücksicht Auf Ihre Anwendung in Der Architektur, vol. 1. Reimer.

Goriely, A., 2017. The Mathematics and Mechanics of Biological Growth. Springer-Verlag.

Goriely, A., Neukirch, S., 2006. Mechanics of climbing and attachment in twining plants. Phys. Rev. Lett. 97, 184302.

Grandgeorge, P., Baek, C., Singh, H., Johanns, P., Sano, T.G., Flynn, A., Maddocks, J.H., Reis, P.M., 2021. Mechanics of two filaments in tight orthogonal contact. Proc. Natl. Acad. Sci. USA 118 (15), e2021684118.

Grason, G.M., 2009. Braided bundles and compact coils: The structure and thermodynamics of hexagonally packed chiral filament assemblies. Phys. Rev. E. 79 (4), 041919.

Howell, H., 1953. The general case of friction of a string round a cylinder. J. Text. Inst. Trans. 44 (8–9), T359–T362.

Jawed, M.K., Dieleman, P., Audoly, B., Reis, P.M., 2015. Untangling the mechanics and topology in the frictional response of long overhand elastic knots. Phys. Rev. Lett. 115 (11).

Johanns, P., Grandgeorge, P., Baek, C., Sano, T.G., Maddocks, J.H., Reis, P.M., 2021. The shapes of physical trefoil knots. Extreme Mech. Lett. 43, 101172.

Jung, J.H., Kang, T.J., Youn, J.R., 2004. Effect of bending rigidity on the capstan equation. Text. Res. J. 74 (12), 1085–1096.

Jung, J.H., Pan, N., Kang, T.J., 2008a. Capstan equation including bending rigidity and non-linear frictional behavior. Mech. Mach. Theory 43 (6), 661–675.

Jung, J.H., Pan, N., Kang, T.J., 2008b. Generalized capstan problem: Bending rigidity, nonlinear friction, and extensibility effect. Tribol. Int. 41 (6), 524–534.

Kirchhoff, G., 1859. Ueber das gleichgewicht und die bewegung eines unendlich dünnen elastischen stabes. J. Reine Angew. Math. 56, 285–313, URL http://eudml.org/doc/147766.

Landau, L., Levich, B., 1988. Dragging of a liquid by a moving plate. Dynamics of Curved Fronts. Elsevier, pp. 141–153.

Landau, L.M., Lifshitz, E.M., 1986. Theory of elasticity. Course Theor. Phys. 7.

Maddocks, J.H., Keller, J.B., 1987. Ropes in equilibrium. SIAM J. Appl. Math. 47 (6), 1185–1200.

Martin, A.J.P., Mittelmann, R., 1946. Some measurements of the friction of wool and mohair. J. Text. Inst. Trans. 37 (12), T269–T280.

Naghdi, P., Rubin, M., 1989. On the significance of normal cross-sectional extension in beam theory with application to contact problems. Int. J. Solids Struct. 25 (3), 249–265.

Panaitescu, A., Grason, G.M., Kudrolli, A., 2017. Measuring geometric frustration in twisted inextensible filament bundles. Phys. Rev. E 95 (5), 052503.

Panaitescu, A., Grason, G.M., Kudrolli, A., 2018. Persistence of perfect packing in twisted bundles of elastic filaments. Phys. Rev. Lett. 120 (24), 248002.

Patil, V.P., Sandt, J.D., Kolle, M., Dunkel, J., 2020. Topological mechanics of knots and tangles. Science 367 (6473), 71–75.

du Peloux, L., Baverel, O., Caron, J.-F., Tayeb, F., 2013. From shape to shell: a design tool to materialize freeform shapes using gridshell structures. In: Design Modelling Symposium Berlin. In: Rethinking Prototyping: Proceedings of the Design Modelling Symposium Berlin 2013, Berlin, Germany.

Poincloux, S., Adda-Bedia, M., Lechenault, F., 2018. Geometry and elasticity of a knitted fabric. Phys. Rev. X. 8 (2).

Poincloux, S., Chen, T., Audoly, B., Reis, P.M., 2021. Bending response of a book with internal friction. Phys. Rev. Lett. 126 (21).

Sano, T.G., Yamaguchi, T., Wada, H., 2017. Slip morphology of elastic strips on frictional rigid substrates. Phys. Rev. Lett. 118, 178001.

Shiryaev, V., Orlik, J., 2015. Modeling of textiles as nets of one-dimensional hyperelastic strings with friction controlled by capstan equation. In: Numerical Methods and Applications. Springer International Publishing, pp. 226–233.

Stoop, N., Wittel, F.K., Herrmann, H.J., 2008. Morphological phases of crumpled wire. Phys. Rev. Lett. 101, 094101.

Stuart, I., 1961. Capstan equation for strings with rigidity. Br. J. Appl. Phys. 12 (10), 559–562, 10.1088%2F0508-3443%2F12%2F10%2F309.

Tu, C.-F., Fort, T., 2004. A study of fiber-capstan friction. 1. Stribeck curves. Tribol. Int. 37 (9), 701–710.

Vekhter, J., Zhuo, J., Fandino, L.F.G., Huang, Q., Vouga, E., 2019. Weaving geodesic foliations. ACM Trans. Graph. 38 (4), 1–22.

Ward, A., Hilitski, F., Schwenger, W., Welch, D., Lau, A.W.C., Vitelli, V., Mahadevan, L., Dogic, Z., 2015. Solid friction between soft filaments. Nature Mater. 14 (6), 583–588.

Warren, P.B., Ball, R.C., Goldstein, R.E., 2018. Why clothes don't fall apart: Tension transmission in staple yarns. Phys. Rev. Lett. 120 (15).

Yoshida, K., Wada, H., 2020. Mechanics of a snap fit. Phys. Rev. Lett. 125.